ACIBADEM MEHMET ALI AYDINLAR UNIVERSITY
INSTITUTE OF HEALTH SCIENCES

DEVELOPMENT OF A TISSUE ENGINEERED *IN VITRO* BLOOD-AIR BARRIER MODEL TO STUDY RESPIRATORY VIRAL INFECTIONS

NEVAL SEVİNÇ ÖZDEMİR
PH.D. THESIS

DEPARTMENT OF MEDICAL BIOTECHNOLOGY

SUPERVISOR
Prof. Vasıf Nejat HASIRCI

SECONDARY SUPERVISOR
Prof. Halime KENAR

ISTANBUL-2024

ACIBADEM MEHMET ALI AYDINLAR UNIVERSITY
INSTITUTE OF HEALTH SCIENCES

DEVELOPMENT OF A TISSUE ENGINEERED *IN VITRO* BLOOD-AIR BARRIER MODEL TO STUDY RESPIRATORY VIRAL INFECTIONS

NEVAL SEVİNÇ ÖZDEMİR

PH.D. THESIS

DEPARTMENT OF MEDICAL BIOTECHNOLOGY

SUPERVISOR
Prof. Vasıf Nejat HASIRCI

SECONDARY SUPERVISOR
Prof. Halime KENAR

ISTANBUL-2024

DECLARATION

I declare that this thesis work is my own work, I had no unethical behavior at any stages from the planning to the writing of the thesis, I obtained all the information in this thesis in accordance with academic and ethical rules, I cited all the information and comments that were not obtained with this thesis work, and I provided resources in the list of references. I also declare that there was no violation of any patents and copyrights during the study and writing of this thesis.

20/11/2024
Neval Sevinç Özdemir

PREFACE AND ACKNOWLEDGEMENT

This study was funded by the Scientific and Technological Research Council of Turkey (TUBITAK) within the scope of Southeast Asia-Europe Joint Funding Scheme for Research and Innovation (SEA-EU JFS) (TUBITAK 1071, Grant No: 121N817). I am sincerely grateful to TUBITAK for their invaluable support and to the Acıbadem University and ACU Biomaterials Center for providing access to their excellent facilities, which made this work possible.

The completion of this doctoral thesis marks an important milestone in my research journey. While my background originally lay in another field, this study broadened my scientific scope, introducing me to a wide array of techniques and concepts that improved my technical skills and creativity. As my theoretical and practical work combined with my observations, it changed my perspective on how tissue engineering naturally intersects with the developmental processes of living organisms, a link often overlooked. Beyond its academic value, this thesis has been integral to my growth as a scientist.

I owe sincere gratitude to those who contributed to this journey. First and foremost, I thank my supervisor, Prof. Vasıf Hasırcı, for introducing me to the tissue engineering as a pioneer of the discipline in my country, and for enabling the realization of this thesis as part of an international collaborative project. I acknowledge my co-supervisor, Prof. Halime Kenar, for her contributions to cell culture studies and for sharing expertise in tissue engineering techniques. I extend my thanks to Prof. Aykut Özkul and his team in Ankara University Virology Department, for enabling the realization of the viral infection studies and for sharing their expertise, which enriched this work significantly.

My deepest appreciation goes to my colleagues and labmates, who were indispensable to this work. I am especially grateful to Gözde Ervin Köle for her invaluable technical contributions, particularly in cell culture, SEM and CLSM imaging, and for her generous guidance on tissue engineering techniques. I am deeply

grateful to Deniz Başöz and Şeyma Işık for their reliable support in the lab, as well as Şimal Yaren Şahin for her continuous assistance and contributions to the lab work of the thesis. I am grateful to all members of the ACU Biomaterials Center for their collaborative spirit and consistent support.

Looking back on this journey, I feel deeply fortunate to have had the support of all the members of the Pharmacy Faculty, especially the Pharmaceutical Basic Sciences Department, where I have been working for many years. My heartfelt thanks go to Prof. Umut Bulut, Dr. Sevgi Sarıgül Özbek, and our Dean, Prof. Mert Ülgen, for their understanding and patience, and unwavering support. Their guidance was instrumental in helping me balance the demands of academic work and research throughout this process.

I would like to express my gratitude to my parents for their nurturing effort to impart in me the values of resilience, integrity, diligence, and ethical responsibility. Their guidance have been the foundation of my character, shaping me into a principled individual who approaches challenges with determination and a strong moral compass. On a deeply personal note, I owe my utmost gratitude to Dr. Özkan Özdemir, my partner, family, best friend, and colleague. His unwavering support, encouragement, and belief in me have been invaluable throughout this journey. Özkan has been my greatest source of strength, inspiration, and creativity, and I am endlessly grateful for his presence in my life.

Completing this thesis has reinforced for me the value of collaboration, perseverance, and support. I leave this chapter of my life with not only a deeper scientific understanding but also profound gratitude for the people who stood by me every step of the way.

TABLE OF CONTENTS

ABBREVIATIONS

3D	Three dimensional
ACE2	Angiotensin converting enzyme 2
AETI	Alveolar epithelial type 1 cell
AETII	Alveolar epithelial type 2 cell
ARDS	Acute respiratory distress syndrome
BAB	Blood-air barrier
BM	Basement membrane
CLSM	Confocal laser scanning microscopy
DAPI	4',6-diamidino-2-phenylindole
ECM	Extracellular matrix
IF	Immunofluorescence (staining)
IM	Interstitial matrix
MTT	3-(4,5-dimethylthiazol-2-yl)-2,5-diphenyltetrazolium bromide
RNA	Ribonucleic acid
RT-qPCR	Reverse transcription quantitative polymerase chain reaction
SEM	Scanning electron microscopy
SNP	Single nucleotide polymorphism
TCP	Tissue culture treated plate
TEER	Transepithelial electrical resistance
TEM	Transmission electron microscopy
WCA	Water contact angle

LIST OF FIGURES

LIST OF TABLES

ABSTRACT

Development Of A Tissue Engineered *In Vitro* Blood-Air Barrier Model To Study Respiratory Viral Infections

This study aims to develop an *in vitro* experimental model that mimics the alveolar blood-air barrier, and to test its ability to simulate native tissue as well as its suitability for studying the interaction between lower respiratory tract viral infections and the barrier components. The model developed in the study contains a thin (<20 μm) electrospun poly(Ɛ-caprolactone) (PCL) membrane with a randomly oriented nanofiber structure to mimic the matrix structure of the basal membrane (BM) found in the barrier. This membrane, coated with collagen type I, fibronectin, and laminin 511 proteins, served as an effective scaffold for the separate adhesion and monolayer formation of alveolar epithelial (A549) and endothelial (pHUVEC) cells on opposite surfaces, allowing for their co-culture through nutrient passage and the formation of an air-liquid interface (ALI). Both cell types exhibited their characteristic phenotypic features on the membrane, and tight junctions were observed between the cells. Permeability tests with molecules of different sizes and transepithelial electrical resistance measurements demonstrated that the model exhibited barrier function by Day 7 after cell seeding. Finally, the model's applicability for viral infection studies was assesed through SARS-CoV-2 infection. The results showed that the developed model is a valuable tool for investigating viral infection mechanisms and interactions occurring at the blood-air barrier, and for testing therapeutic approaches.

Keywords: Blood-Air barrier, Tissue Engineering, 3D Tissue Models, *In Vitro* models, COVID-19.

ÖZET

Solunum Yolu Viral Enfeksiyon Çalışmalarında Kullanılmak Üzere Doku Mühendisliği Yöntemiyle Bir *In Vitro* Kan-Hava Bariyeri Modeli Geliştirilmesi

Bu çalışma, alveolar kan-hava bariyerini taklit etmek üzere bir *in vitro* deney modeli geliştirmeyi, bu modelin gerçek dokuyu taklit etme yeteneğini ve alt solunum yolu viral enfeksiyonları ile bariyer bileşenlerinin etkileşimini çalışmak için uygunluğunu test etmeyi amaçlamaktadır. Çalışmada geliştirilen model kan-hava bariyerinde bulunan bazal membranın (BM) matriks yapısını taklit etmek için rasgele yönlü nanofiber yapısına sahip, ince (<20 μm) bir elektroeğrilmiş poli(ε-kaprolakton) (PCL) ağ membran içermektedir. BM yapısında bulunan kolajen tip I, fibronektin ve laminin 511 proteinleri ile kaplanan bu membran, alveolar epitel (A549) ve endotel (pHUVEC) hücrelerinin birbirlerinden ayrılmış halde karşılıklı yüzeylere tutunması, tek tabaka halinde çoğalması, besin geçişine izin vererek hücrelerin ortak kültürü ve hava-sıvı arayüzü (ALI) oluşturulması için etkili bir zemin görevi görmüştür. Her iki hücre tipi de karakteristik fenotipik özelliklerini membran üzerinde göstermiş ve hücreler arasında kurulan sıkı bağlantılar gösterilmiştir. Farklı boyutlu moleküllere karşı yapılan geçirgenlik testleri ve transepiteliyal elektriksel direnç ölçümleri modelin hücre ekiminden sonra 7. gün itibariyle bariyer işlevine sahip olduğunu göstermiştir. Son olarak, modelin viral enfeksiyon çalışmalarında kullanılabilirliği SARS-CoV-2 enfeksiyonu gerçekleştirilerek incelenmiştir. Elde edilen sonuçlar, geliştirilen bu modelin kan-hava bariyerinde gerçekleşen viral enfeksiyon mekanizma ve etkileşimlerini incelemek ve terapötik yaklaşımları denemek için değerli bir araç olduğunu göstermiştir.

Anahtar Sözcükler: Kan-Hava Bariyeri, Doku Mühendisliği, 3B Doku Modeli, *In Vitro* Modeller, COVID-19.

1 INTRODUCTION

1.1 Critical Role of the Blood-Air Barrier in Viral Pneumonia

The blood-air barrier (BAB) of the human lung serves two critical functions crucial for survival. First, it facilitates the transfer of oxygen from the lung to the bloodstream and the removal of carbon dioxide from the blood to air. All this happens across the thin, selectively permeable structure that separates the air in the alveoli from the blood in the surrounding capillaries. This is vital for efficient respiratory function and overall metabolic health. Second, its lipid surfactant layer serves as a protective shield, which prevents alveolar collapse during breathing and contains immunomodulatory proteins against airborne pathogens, including respiratory viruses causing pneumonia. Increased severity and morbidity in viral pneumonia primarily result from the progression of infection to the area, and the most severe clinical presentations arise upon the disruption of the barrier integrity. Infection of the alveolar epithelium of the BAB leads to the recruitment of immune cells to the area, and leads to severe inflammation, edema, and thickening of the barrier, escalating to acute respiratory distress syndrome (ARDS), which may progress into multi-organ failure.

1.2 The Need for an Advanced *in vitro* Barrier Model

The Coronavirus Disease 2019 (COVID-19) pandemic has highlighted that understanding the interactions between respiratory viruses and the BAB is fundamental for the development of therapeutic approaches and preventive measures. Traditional models developed to study these interactions have relied heavily on simplified *in vitro* cultures which do not fully replicate human physiological responses. Various *in vitro* models such as epithelial air-liquid interface (ALI) models, tissue engineered barrier models, and lung-on-chip systems, have shown promise in mimicking the complex lung microenvironment. Among the models developed so far, ALI models have been used widely as they are simple, rapid, and cost-effective, however, lack structural and biochemical complexity. Tissue engineered barrier models are more relevant in complexity but require significant expertise. Lung-on-

chip systems aim to introduce organ-level functions into a microfluidic device by trying to simulate the microphysiology of the human lung, by mimicking cyclic mechanical forces and blood flow dynamics. Membranes are a crucial component of those systems as they have a significant control over the physical and mechanical properties, such as porosity, thickness, and elasticity, which eventually control transference across the barriers. As such, these membranes must meet the complex structural and functional properties of the basement membrane of the native BAB. Recent advances in tissue engineering, featuring diverse polymeric scaffolds, cell types, and extracellular matrix components have paved the way for developing more complex and physiologically relevant *in vitro* models. Such models offer the potential to be combined with microfluidic systems, mimicking the human BAB more accurately, and providing a platform to study viral pathogenesis, host responses, and the efficacy of potential treatments. Despite these advances, generating a tissue engineered BAB model that adequately represents the human BAB is still a major challenge.

1.3 Objective, Significance, and Contribution to Science

The primary objective of this thesis is to develop a tissue engineered model of the human BAB that closely mimics its properties *in vitro*. The model aims to combine accessibility and ease of construction while preserving the intricate architecture of the native basement membrane of the BAB. It was designed to offer a precise, microfluidic-compatible tissue model that closely mimics the alveolar environment enabling researchers to study host-pathogen interactions and test antiviral compounds or other therapeutic approaches.

This model offers several benefits including:

- Enhanced structural and biological relevance: Incorporates key features of the human BAB, particularly its microstructure and composition, to provide more accurate pre-clinical test results, facilitating improved translation into clinical applications.

- Reduction in animal testing: Provides a reliable alternative *in vitro* model, reducing the need for animal models and supporting ethical research practices.

- Contribution to the rate of drug screening: Facilitates rapid screening of antiviral compounds, thus accelerating the development of effective therapies against respiratory viruses.

- Contribution to the efforts against global pandemics: Expands accessible, cost-effective models, supports global research efforts, and addresses challenges of model availability and affordability.

This thesis presents a novel *in vitro* BAB model positioned between conventional cell culture and animal studies. It was shown that it serves as a reliable platform for viral pneumonia research, including virus-barrier interactions, infection dynamics and pathogenesis, and host immune responses. It facilitates the integration of tissue engineered barrier models with microfluidic (on-chip) systems, improving the relevance of *in vitro* models to native biological systems. Additionally, it can serve in the development of personalized treatment protocols and as a platform for developing and testing therapeutic agents, thus shorten the time for translation into clinical applications.

2 BACKGROUND

2.1 Human Respiratory System

The human respiratory system is organized as a series of tubular sections channeling the air from the nose or mouth to the lung tissue. It is divided into upper and lower airways, which further branch into the lung tissues. The upper airways consist of the nasal passages, pharynx, and larynx, which filter and humidify inhaled air before it reaches deeper into the lower airways. Lower airways start with the trachea, which branches into two main bronchi, and then divides into smaller bronchioles. These bronchioles direct air to the alveolar ducts and finally to the alveoli, where O_2 and CO_2 exchange takes place (Figure 1). This branching provides progressively smaller segments as they reach the lung tissue, maximizing the surface area available for effective gas exchange. The trachea is supported by hyaline cartilage which is connected to a smooth muscle tissue, which continues to encircle the bronchi and bronchioles made of an elastic tissue rather than hard cartilage. This structure allows for controlled flexibility and dilation in the airways, enhancing the respiratory system's response to varying air demands (9-12).

The lungs contain approximately 500 million alveoli, each about 1/3 mm in diameter, separated by thin walls of the alveolar septa, creating a large surface area of 50 to 100 m^2 for gas exchange. Although only a few millimeters span from the terminal bronchiole to the outermost alveolus, the respiratory zone constitutes the majority of the lung's volume, about 2.5 to 3 liters at rest. Inspiration enlarges the volume of the thoracic cavity as the diaphragm contracts and descends, and the action of intercostal muscles raises the ribs, increasing the thorax's cross-sectional area. Air is then drawn into the lungs and moves down to the terminal bronchioles by bulk flow, with diffusion being the primary mechanism of ventilation in the respiratory zone (13, 14).

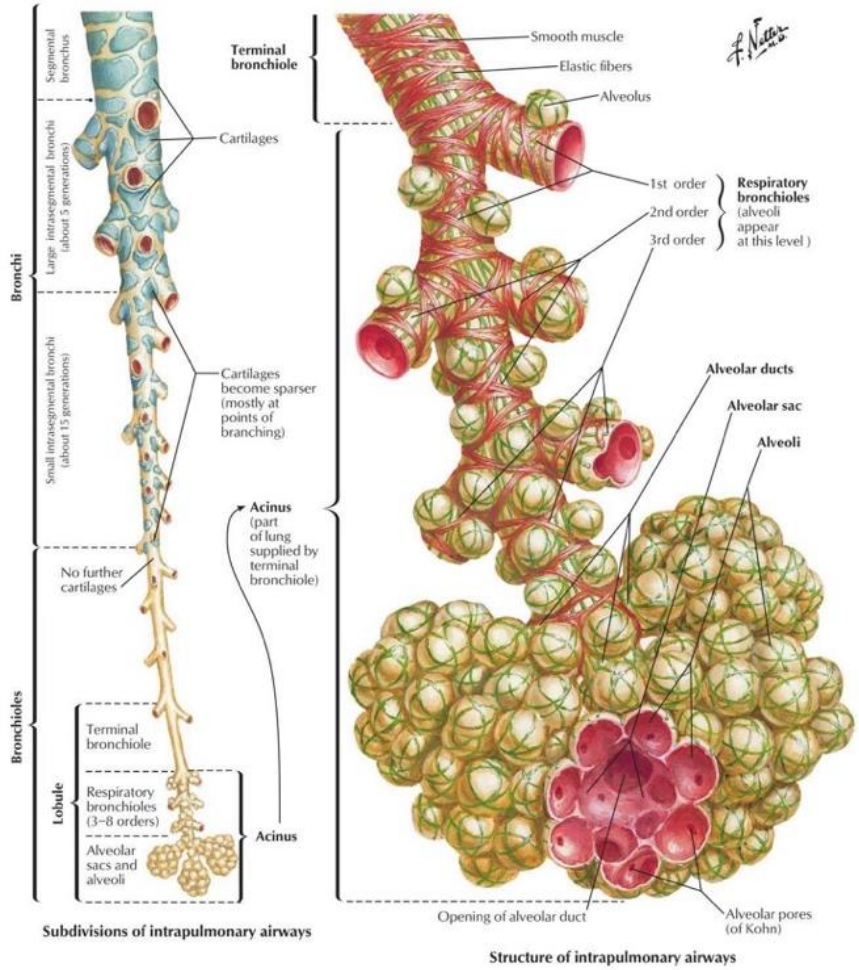

Figure 1 Subdivisions and structure of intrapulmonary airways (1)

The pulmonary blood vessels, pulmonary arteries, and pulmonary veins comprise a specialized network facilitating blood flow to and from the lungs. Pulmonary arteries carry O_2-poor blood from the right ventricle of the heart to the lungs for oxygenation and CO_2 removal. These arteries have thin and elastic walls, allowing them to expand and contract as blood flows through them, accommodating the dynamic pressures during the cardiac cycle. Conversely, pulmonary veins return O_2-enriched blood from the lungs to the left atrium of the heart. These veins possess wider and more flexible walls compared to pulmonary arteries, enabling them to accommodate large volumes of blood returning to the heart (15, 16). Both pulmonary arteries and veins are connected to a dense network of capillaries embedded within the alveolar walls. These capillaries form a continuous sheet-like network across the alveolar wall which provides the site for the gas exchange between the blood and the alveoli (Figure 2).

This structural feature ensures that red blood cells transit closely to the alveolar gas, enhancing the efficiency of O_2 uptake and CO_2 release. These capillary segments, typically ranging from 7 to 10 μm in diameter, are so narrow that they allow just enough space for a single red blood cell at a time. Each red blood cell spends about 0.75 seconds within the capillaries, during which it presumably passes through 2-3 alveoli. This rapid time of transit, coupled with the optimized anatomical structure allows for nearly complete equilibrium of O_2 and CO_2 levels between the alveolar gas and blood within the capillaries. This is critical for maintaining high metabolic demands during various physiological states of the body (15, 17, 18).

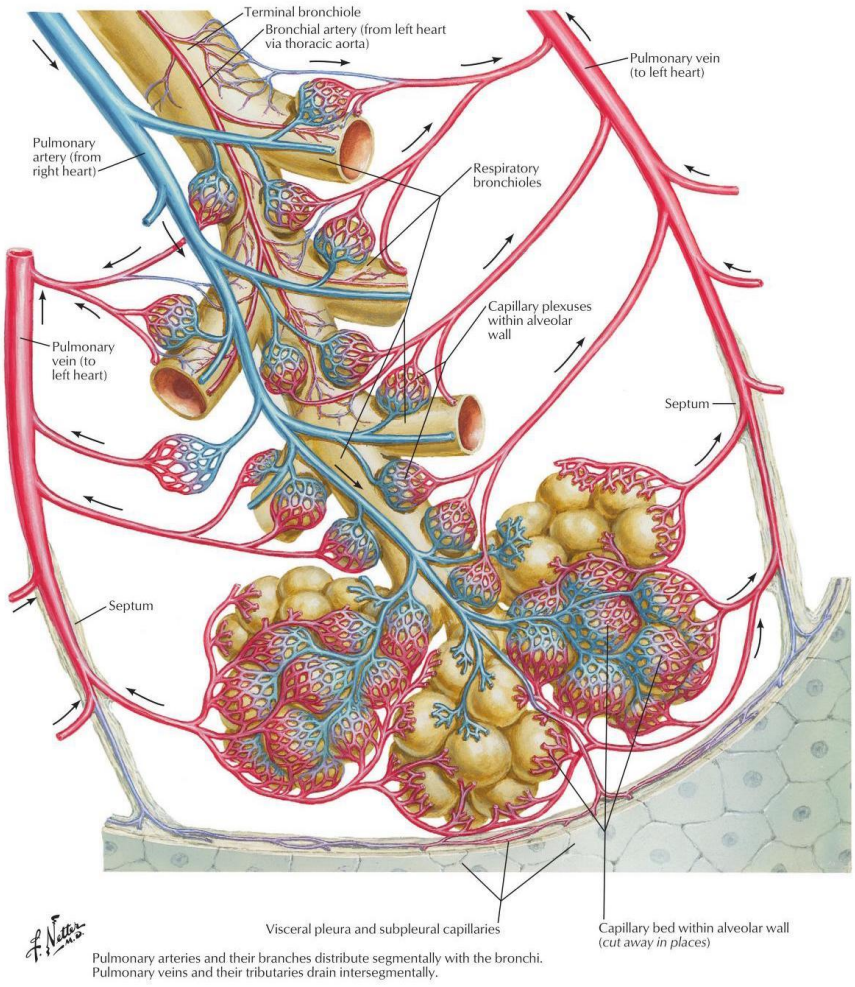

Figure 2 Scheme of the intrapulmonary blood circulation (9)

Along with its complex branched structure providing efficient ventilation and gas exchange, human respiratory system employs various defense systems against airborne pathogens and pollutants to maintain its optimal function. These systems protect the structural components extending from nasal cavities to the alveoli. The alveolar gas interface is the most remote point of access for airborne particles and functions akin to the latest gatekeeper between the inhaled air and the blood flow. The next section will detail the structure, composition, and function of this critical interface, known as the "Blood-Air Barrier" ("Air-Blood Barrier", "Alveolocapillary Membrane", MeSH Unique ID: D015824).

2.2 The Blood-Air Barrier

The blood-air barrier (BAB) is a remarkably thin (0.5 to 1.5 μm), complex, and resilient tissue interface that is vital for the exchange of gases between the alveolar air and the bloodstream. It is composed of alveolar epithelial cells (pneumocytes) covered by alveolar lining fluid, a fused basement membrane with an interstitial space containing connective tissue and extracellular matrix (ECM) components, and pulmonary microvascular endothelial cells lining the capillaries on the opposite side (Figure 3, Figure 4). It acts as a selectively permeable filter allowing the passage of molecules from one side to the other while providing a large surface area for the rapid diffusion of gases (18-20). It holds the key events for sustainable cellular respiration: the uptake of O_2 which is essential for aerobic ATP production, and the removal of CO_2, a byproduct of the Krebs cycle, which is critical for maintaining the blood pH balance. Proper functioning of the BAB is central to overall metabolic health and plays a critical role in regulating the cascade of immune responses during pulmonary infections (12, 16, 19, 21-23).

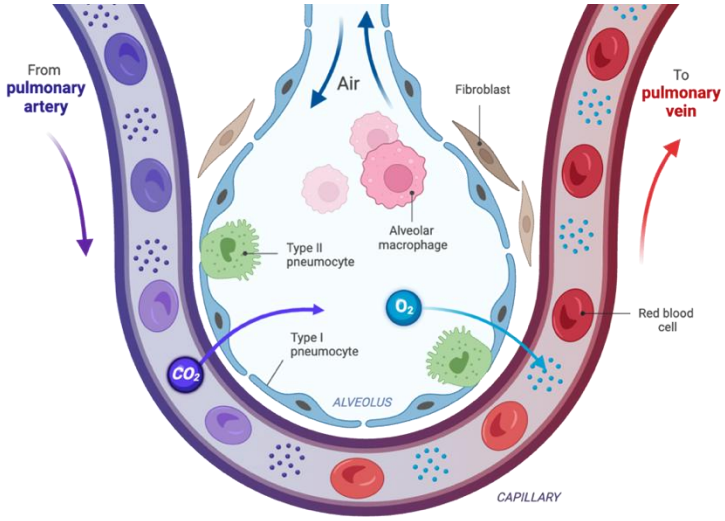

Figure 3 Illustration of alveolar gas exchange across the blood-air barrier

2.2.1 Structure and composition

Human BAB is composed of alveolar epithelial cells with the alveolar lining fluid over the epithelium, pulmonary microvascular endothelial cells, and a basement membrane in between with an interstitial space containing connective tissue and extracellular matrix (ECM) components (Figure 4).

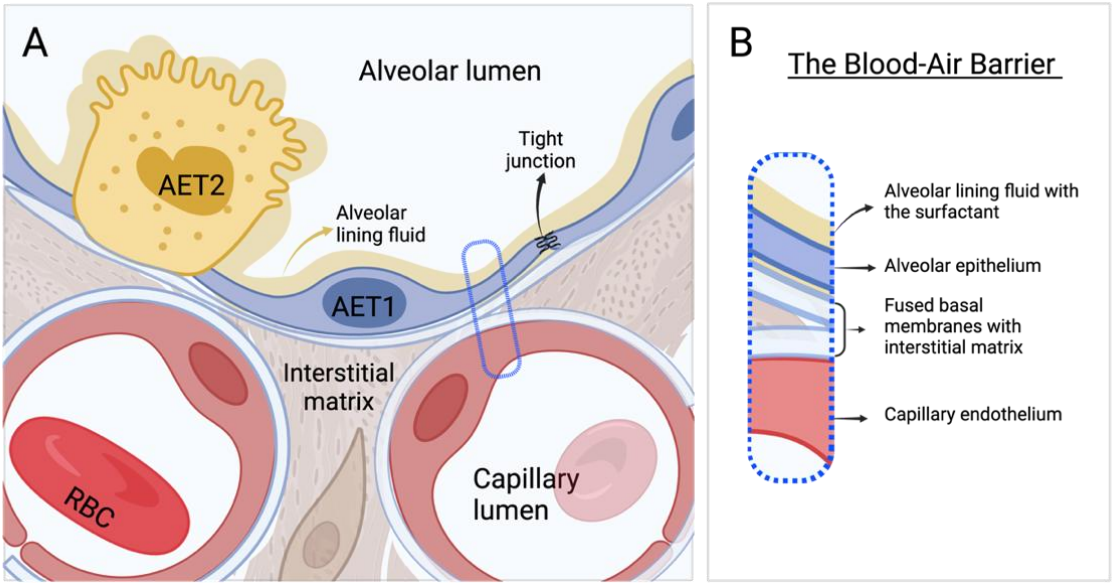

Figure 4 Structural overview of the BAB. A) Alveolar-capillary interface, *AET1 and AET2:* Alveolar epithelial type I and type II cells, *RBC:* Red blood cells in the capillary lumen. B) A cross-sectional view of the BAB, illustrating the diffusion pathway for gases across these structures.

2.2.2 Basement membrane and interstitial ECM

The basement membrane (BM) of the BAB is a fused layer of epithelial and endothelial basal membranes containing the interstitial ECM, yet with a thickness of 100 - 200 nm. It acts as a physical barrier with its a porous structure allowing for the selective passage of gases, nutrients, waste products, and cell signaling molecules between the two layers (12, 24-26). Measuring the pore size of the BM is challenging due to its complex structure composed of ECM components which vary in size and shape. Additionally, the dynamic nature of the BM composition alters both its chemical and physical properties in response to environmental stimuli. However, in a healthy state, it is well known that the permeability of BM is determined by the size, charge, and shape of the molecules that pass through it. While small, uncharged molecules such as O_2, CO_2, and small solutes diffuse easily, larger and charged molecules such as plasma proteins are restricted and might require specialized transport mechanisms (12, 27, 28).

The interstitial matrix (IM) in the BM is a complex network of structural proteins, glycoproteins, and proteoglycans, which collectively contribute to the barrier's structural integrity and mechanical strength while modulating cell-matrix interactions that are pivotal for biological signaling processes (Figure 5) (5, 29-33). **Collagens** are the most abundant structural proteins in the BM, primarily responsible for barrier's structural integrity and resilience to volume changes during breathing. Type IV collagen is the most abundant structural protein which forms a network crucial for the filtration capability and selective permeability of the BAB (4, 34, 35). Type I collagen, characterized by tightly packed fibers, offers rigidity and mechanical stability to the alveoli. It is associated with type V collagen which regulates the diameter and assembly of its fibers. Type III collagen enhances flexibility and resilience, allowing lung tissue to endure the cyclic stretching movements. Type VI collagen forms a beaded filament structure, helping to anchor the cells to the BM primarily via integrins and chondroitin sulfate proteoglycan 4 (NG2) (36-40). **Elastin** is another critical structural protein which facilitates the stretching and recoiling of lung tissue during the respiratory cycles. Elastin fibers interact with collagens and other ECM

components to create a flexible yet stable framework, ensuring the rapid reinflation of air spaces post-exhalation (5, 41, 42).

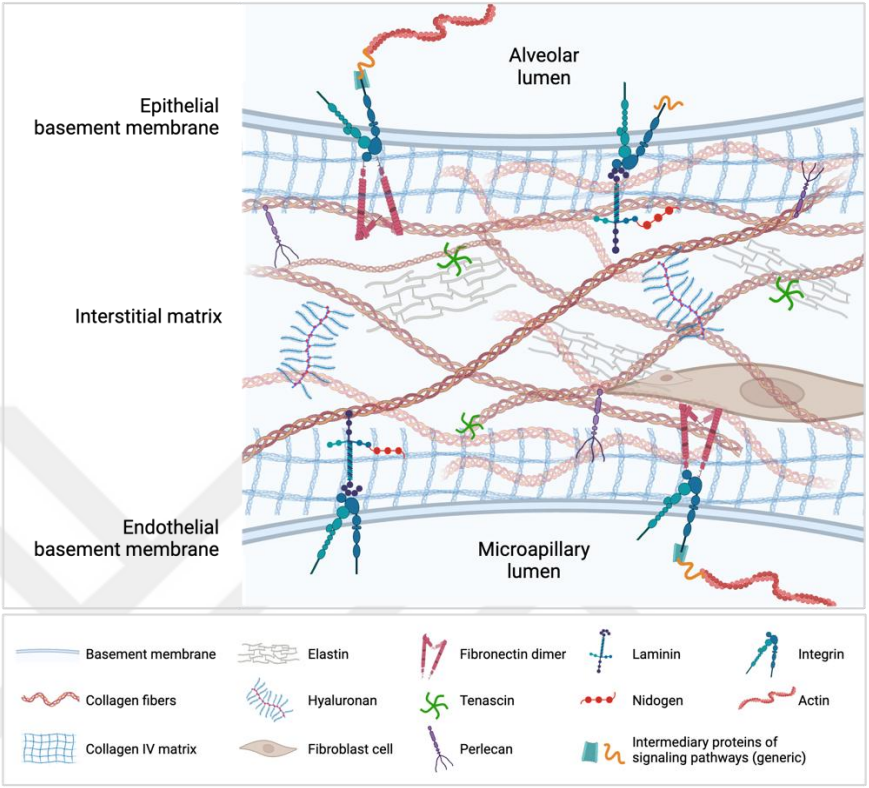

Figure 5 Detailed illustration of the interstitial matrix components composed of various extracellular matrix proteins (4, 5).

Glycoproteins, such as laminins, fibronectin, and nidogen, are crucial for cell adhesion to the BM and signal transduction across the barrier (32, 36, 41). **Laminins** are critical for anchoring cells to the membrane by interacting with integrins and other cell surface receptors, facilitating cellular differentiation and migration. The most abundant isoforms of laminin in BAB are laminins 511 and 411, responsible for transducing environmental stimuli, such as mechanical forces and injury, into an intracellular cascade of molecular events (32, 43). **Fibronectin** is also critical for cell adhesion as it interacts with cell surface receptors while binding to collagen fibrils. This dual binding is central for collagen fibrillogenesis and ECM organization, as well as the modulation of collagen deposition, thus playing a key role in tissue remodeling and pulmonary repair (37, 44, 45). **Nidogen,** also known as entactin, integrates laminins and collagen type IV to create a coherent network by linking them through

its filamentous structure (46). In summary, glycoproteins in BM collectively ensure its stability and functionality, playing critical roles in cell adhesion, tissue repair, and structural integrity (47).

Proteoglycans are subtype of glycoproteins with a larger carbohydrate component made up of one or more specific glycosaminoglycan (GAG) chains giving unique biochemical properties and functions to them (29, 48). **Perlecan** is one of the most abundant proteoglycans in the BAB, which has heparan sulfate chains that not only contribute to the charge-selective permeability of the BM, but also modulate the availability of growth factors by stabilizing them through direct interactions (49, 50). **Tenascin** affects cell migration through the specific signaling domains in its hexameric structure which create anti-adhesive properties. In addition, its elastic and flexible structure allows it to function as a versatile scaffold during dynamic processes occurring in its microenvironment (51). Another important component of the BAB ECM is **hyaluronan**, which provides hydration and contributes to the structural integrity of the ECM. Unlike other GAGs, hyaluronan does not bind to a protein core and exists as a free GAG. Hyaluronan production balance is particularly important in case of pneumonia progression as its excessive production creates a more fibrotic environment, thus altering the ECM composition. This alteration causes the sequestering of more immune cells, exacerbating inflammation and causing the thickening of the BAB (52).

In summary, the basement membrane structure is the key component of the BAB, containing various types of interstitial matrix proteins with their unique features, providing structural and functional integrity, filtering the air and blood, and adapting to physiological and pathological changes. Mimicking the collagen type IV matrix is critical to accurately replicate the permeability of the basement membrane (33, 35). The structural integrity is typically mimicked using collagen type I, along with fibronectin and laminins which interact with cell surface receptors like integrins. Any alteration in its composition potentially leads to compromised barrier integrity, thus considered a critical factor in the pathology of various lung diseases, including viral

pneumonia. These interactions provide structural support by attaching to the cytoskeleton via actin filaments and facilitate signal transduction pathways (53-55).

2.2.3 Cells, surfactant layer and glycocalyx

The cells of the BAB are positioned on the basement membrane, with epithelial and endothelial cells forming monolayers on opposite sides. The epithelial cells face the air, and capillary endothelial cells face the blood flow. There are 2 types of **alveolar epithelial cells,** or pneumocytes: Alveolar epithelial type I (AETI) and type II (AETII) cells (Figure 6). AETI cells cover approximately 90-95% of the alveolar surface area, despite constituting only about 40% of the alveolar epithelial cell population. These cells are exceptionally thin (100 – 500 nm) and can be 50 - 100 μm in diameter. This thin, squamous, monolayer structure of the alveolar epithelium is specialized to minimize the travel distance of O_2 and CO_2 during gas exchange (56). AETI cells have cytoplasmic extensions that form tight cell to cell junctions, creating a continuous barrier. These tight junctions are crucial in maintaining the size and charge dependent permeability of the BAB, preventing leakage of fluids and solutes between the alveolar space and the bloodstream. The tight junction complex includes several key proteins, such as claudins (especially claudin-3, claudin-4, and claudin-18), occludin, and junctional adhesion molecules (JAMs). These proteins interact to seal the paracellular space and regulate the passage of molecules (57, 58). Unlike the squamous AETI cells, AETII cells have a cuboidal morphology with prominent multilayered inclusions known as multilamellar bodies (MLBs) which are rich in phospholipids and surfactant proteins (3, 57). AETII cells are essential for maintaining lung function due to their two primary features: they have the ability to differentiate into AETI cells, thus can regenerate the alveolar epithelium and repair alveolar damage, and they possess the specialized organelles MLB that produce the surfactant - a lipid-protein mixture that lines the alveolar epithelium reducing surface tension at the air-liquid interface, preventing alveolar collapse during exhalation. The release of surfactant by the MLBs into the alveolar space is mainly triggered by mechanical stimuli caused by breathing (59-61). After secretion, surfactant components are recycled by AETII cells, where surplus material can be either degraded or reutilized for new surfactant synthesis (62).

These multifunctional properties make AETII cells indispensable for maintaining alveolar stability and efficiency in gas exchange (57, 63).

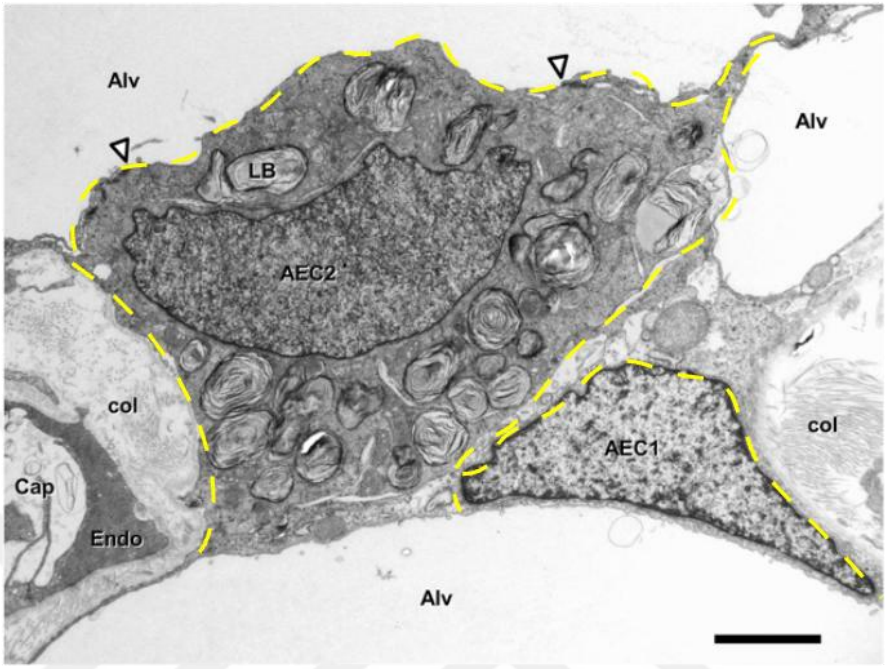

Figure 6 TEM micrograph of the alveolar septum with type I (AEC1) and type II (AEC2) alveolar epithelial cells (3). *LB:* lamellar bodies, *col:* collagen fibrils in the interstitium, *Endo:* capillary endothelial cell, *Alv:* alveolar lumen, *Cap:* capillary lumen. Arrowheads mark the tight junctions between AECII and AECI cells. Yellow dashes indicate the cell borders. Scale bar 2 μm.

The pulmonary surfactant is distributed within an aqueous medium called the alveolar lining fluid (ALF), which covers the alveolar epithelium to maintain the air-liquid interface (ALI). The ALF provides a moist environment that protects lung tissue from any damage caused by dry or cold air. Its composition is tightly regulated to balance electrolytes, proteins, and other solutes dissolved in water. Alterations in ALF volume or composition can impair surfactant function: while excessive ALF dilutes the surfactant and decreases its effectiveness, insufficient ALF hampers its distribution and functionality (64, 65).

Phosphatidylcholine (PC) comprises 70-80 % of the surfactant and is essential for reducing surface tension due to its amphipathic properties. In the ALF, PC molecules form a cohesive film with hydrophobic tails facing the air and hydrophilic heads facing

the water. Dipalmitoyl phosphatidylcholine (DPPC) is the most abundant form of PC in the surfactant, forming a densely packed, stable monolayer that effectively reduces surface tension. Other forms of PC such as palmitoyloleoyl phosphatidylcholine (POPC) with unsaturated fatty acids enhance the fluidity and spreadability of the surfactant across the epithelium. Sphingomyelin (SM) constitutes 10-15% of the surfactant, helping its dense packing and contributing to the robustness of the layer to resist stress during respiratory cycles. Cholesterol also aids in stability and fluidity, making up about 5% of the surfactant. The small hydrophobic proteins in the surfactant, surfactant protein B (SP-B) and SP-C, maintain proper alignment of phospholipids and facilitate rapid adsorption and redistribution of surfactant during the respiratory cycles (66-68). The combination of these components ensures the surfactant's effectiveness in reducing surface tension, its mechanical stability, and proper distribution across the epithelium (3, 61, 69, 70). The other critical duty of the surfactant is to contribute to the immune defense of the alveoli (71, 72). SP-A is an immunomodulatory protein that opsonizes the particulates, supporting the activation of the alveolar macrophages to clear them by phagocytosis. SP-D directly binds to pathogens covering their surface to neutralize them and present them to immune cells. The expression levels of these immunomodulatory proteins are known to be upregulated in response to pulmonary infection (72-74).

Pulmonary microvascular endothelial cells (PMECs) line the inner surface of the capillaries surrounding the alveoli. Like alveolar epithelial cells, PMECs are exceptionally thin (100-500 nm) and are 10-20 μm in diameter, facilitating efficient gas exchange across the barrier (48, 75). Their primary role is to balance the fluid transfer across the BAB, ensuring efficient gas transfer while acting as a selective barrier against molecules such as lipoproteins and blood components. Additionally, PMECs regulate vascular tone by contributing to the contraction and dilation of blood vessels, thus maintaining proper blood flow in the lungs (48, 75-77). PMECs form adherence junctions (AJs) using proteins such as VE-cadherin, β-catenin, and p120-catenin. AJs stabilize intercellular connections, regulate permeability, and respond to mechanical and inflammatory stimuli, maintaining the integrity and selective permeability of the BAB (75, 78). The **endothelial glycocalyx** further supports these

roles of PMECs. It is a layer of glycoproteins and proteoglycans covering the surface of the endothelium, providing anticoagulant properties by binding to antithrombin III and other coagulation inhibitors (61, 79). It inhibits the adhesion of pathogens and harmful substances by shielding the endothelium and limits the adhesion of leukocytes and platelets to the capillary walls by masking adhesion molecules, thereby preventing the initiation of inflammatory responses (48, 80). The glycocalyx acts as a transmitter of mechanical stimuli, while shielding PMECs from shear stress exerted by blood flow (76, 81).

Alveolar macrophages (AMs) are immune cells located in the alveoli, acting as sentinels within the surfactant layer via their microvilli. They serve as the primary immune defense within the alveolar space by entrapping airborne particles that reach the alveolar space. They secrete cytokines and chemokines such as tumor necrosis factor-α (TNF-α) and interleukin-1β (IL-1β), which are critical modulators of the early stages of inflammation and orchestrating the activities of other immune cells in the lung. AMs assist in the clearance of cell debris and recycling of phospholipids and proteins of the surfactant, contributing to the turnover of its components (82-84). Efficient functioning of the AMs significantly affects the integrity and functionality of the BAB, especially in conditions where the BAB is compromised, such as ARDS and chronic obstructive pulmonary disease (COPD). They help mitigate further damage in these conditions and facilitate the repair processes for restoring normal lung function (85, 86).

Pulmonary fibroblasts form a connective tissue containing the interstitial ECM of the BAB. They are critical for the production and remodeling of the ECM, which makes them primary responsible of pulmonary fibrosis, where they become overactive and cause excessive ECM deposition and tissue scarring (87). Fibroblasts contribute to the regulation of vascular permeability by interacting with endothelial cells to prevent excessive fluid leakage into the alveoli (39). They also respond to mechanical stimuli and contribute to the repair of epithelial and endothelial monolayers after injury (5, 88).

2.2.4 Functionality in pulmonary gas exchange

The functionality of the BAB in pulmonary gas exchange is fundamental to maintaining efficient uptake of O_2 and elimination of CO_2 driven by coordinated mechanics of the lung and diaphragm. During inhalation, the diaphragm contracts and moves downward, increasing thoracic cavity volume and thereby decreasing intrapulmonary pressure. This action creates a difference between atmospheric and alveolar pressures, allowing the air to flow into the lungs and fill the alveoli with O_2-rich air. During exhalation, the diaphragm relaxes and moves upward, reducing thoracic cavity volume and thereby increasing intrapulmonary pressure and pushing air out of the lungs to expel CO_2. The BAB serves as the interface of gas exchange, providing a large surface area for the efficient transfer of gases between alveolar air and pulmonary capillary blood. Key characteristics of the barrier, such as its minimal thickness and extensive surface area, ensure that O_2 rapidly diffuses from alveoli into the bloodstream, where it is transported to body cells for cellular respiration. Concurrently, CO_2, a metabolic byproduct, is transported from the cells into the bloodstream where it diffuses into the alveoli (Figure 7) (89-91).

The primary mechanism for this gas exchange is passive diffusion, driven by partial pressure gradients of O_2 and CO_2. Oxygen has a higher partial pressure in the alveoli (PAO_2), typically around 100 mmHg, compared to capillary blood where it is approximately 40 mmHg, enabling its passive diffusion from alveoli to blood through BAB. Conversely, carbon dioxide has a higher partial pressure in the blood (around 45 mmHg), driving its passive diffusion into the alveoli (where $PACO_2$ is about 40 mmHg). Rhythmic contractions and relaxations of the diaphragm drive these pressure differences (10, 21, 23, 33, 90, 92).

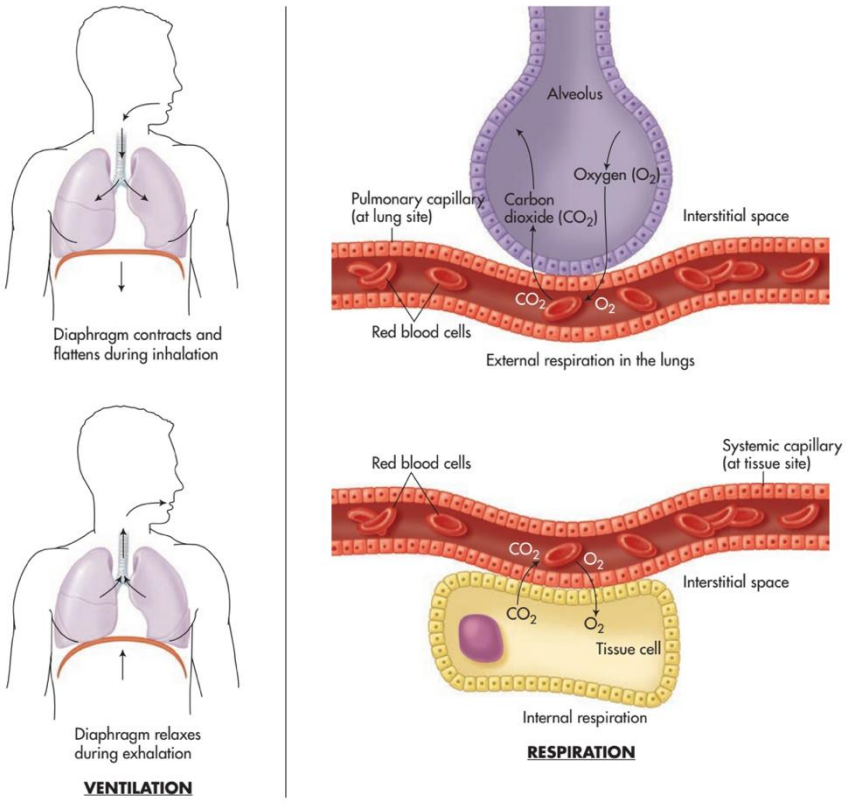

Figure 7 Gas exchange through the BAB (8)

Under resting conditions, approximately 250 mL of O_2 and 200 mL of CO_2 are exchanged per minute across the BAB. These rates increase significantly during exercise to meet the body's heightened metabolic demands. Normal expiration is passive due to elastic recoil of the lung and thoracic cage, while forced expiration involves active contraction of abdominal and intercostal muscles to further increase thoracic pressure. The BAB exemplifies an optimal balance of minimal diffusion resistance and mechanical robustness. This intricate system underscores the complexity and adaptability of the respiratory process, ensuring sufficient gas exchange to sustain physiological functions (13, 19, 89, 93, 94).

2.3 Alveolar Defensive Mechanisms

Atmospheric pollutants, including carbon monoxide, hydrocarbons, sulfur and nitrogen oxides, particulates, and photochemical oxidants, are deposited in the respiratory tract based on their size. Particles larger than 5 μm are trapped in the nasopharynx by impaction, medium-sized particles (1–5 μm) settle in the small airways through sedimentation, and particles smaller than 0.1 μm diffuse into the alveoli. Two primary mechanisms clear these deposited particles: In the upper airways, the mucociliary system employs the mucociliary escalator action of bronchial cilia to move particles to the gastrointestinal tract via the nasopharynx. In the alveoli, where cilia and mucus are absent but transitioned into the surfactant layer, alveolar macrophages (AMs) are responsible for clearing particles by phagocytosis (91, 95-97). Inhaled pathogens reaching alveoli encounter AMs through their pathogen-associated molecular patterns (PAMPs), resulting in their activation through Toll-like Receptors (TLRs) or other pattern recognition receptors (PRRs). AMs can engulf and digest various pathogens, including bacteria, viruses, and fungi, within phagosomes which is then fused with lysosomes, forming phagolysosomes for degradation. Activated AMs release pro-inflammatory cytokines such as IL-1β, IL-6, and TNF-α, and chemokines including CXCL9, CXCL10, and CCL5, which recruit neutrophils and lymphocytes to the infection site. On the other hand, AMs also produce anti-inflammatory mediators such as TGF-β and IL-10 to regulate the inflammation and prevent excessive tissue damage caused by exacerbated immune response. Clearance of apoptotic cells and debris is also employed by AMs while coordinating tissue remodeling processes (85, 98, 99).

AETs and AMs interact closely through both direct cell-cell contact and soluble factors to regulate immune responses. The pulmonary surfactant proteins secreted by AETII cells, particularly SP-A and SP-D, block TLR signaling and inhibit complement activation, thus preventing excessive inflammation (100). The phagocytic ability of AMs is enhanced by these proteins by interacting with signal-regulatory protein-α (SIRPα) to balance phagocytosis and regulate macrophage activation. On the other hand, activation of AMs is inhibited through the binding of AETII protein CD200 to

its receptor on AMs (CD200R), which limits the activation of the pathways such as extracellular signal-regulated kinase (ERK), JUN N-terminal kinase (JNK), and p38 mitogen-activated protein kinase (MAPK) (99, 101). Additionally, AETI cells produce transforming growth factor-beta (TGF-β), which regulates macrophage function and promotes anti-inflammatory responses (102, 103). The balance between the pro- and anti-inflammatory factors in the alveoli ensures a balanced immune response, preventing excessive inflammation while allowing effective defense against pathogens (82, 104).

2.3.1 Respiratory viral infections and blood-air barrier

Respiratory viruses are a group of pathogens that typically spread through respiratory droplets, primarily targeting the respiratory tract, causing diseases that range from mild colds to severe pneumonia. Some of the most well-known respiratory viruses include influenza virus, which causes seasonal outbreaks with high rates of morbidity and mortality; respiratory syncytial virus (RSV), a major cause of respiratory infections in infants and the elderly; and severe acute respiratory syndrome coronavirus 2 (SARS-CoV-2), the novel coronavirus behind the COVID-19 pandemic, which has had an unprecedented global impact. Additionally, rhinoviruses, adenoviruses, and other coronaviruses contribute to the worldwide burden of respiratory infections. Their adaptive ability to evade mucociliary clearance and set back the host immune response at the site of infection can cause widespread damage to the epithelial cells lining the respiratory tract, progressing with excessive rates of inflammation, which in severe cases can lead to serious lung damage (105, 106).

Respiratory viruses initiate infection by attaching to specific surface receptors on the host cells' membrane. For example, SARS-CoV-2 binds to angiotensin-converting enzyme 2 (ACE2) via its spike (S) protein to enter the host cell through endocytosis or membrane fusion, allowing its RNA to access the host's cellular machinery (Figure 8). The infection typically begins in the upper respiratory tract, where the virus infects nasal epithelial cells, including ciliated cells and goblet cells that express high levels of ACE2 (6, 7). As the virus replicates it causes cellular damage and apoptosis,

reducing the effectiveness of mucociliary clearance and evading this protective barrier, releasing newly produced viral particles that can spread to the lower respiratory tract, and ultimately reach the distal lungs where alveoli and the BAB are located (6, 7, 107).

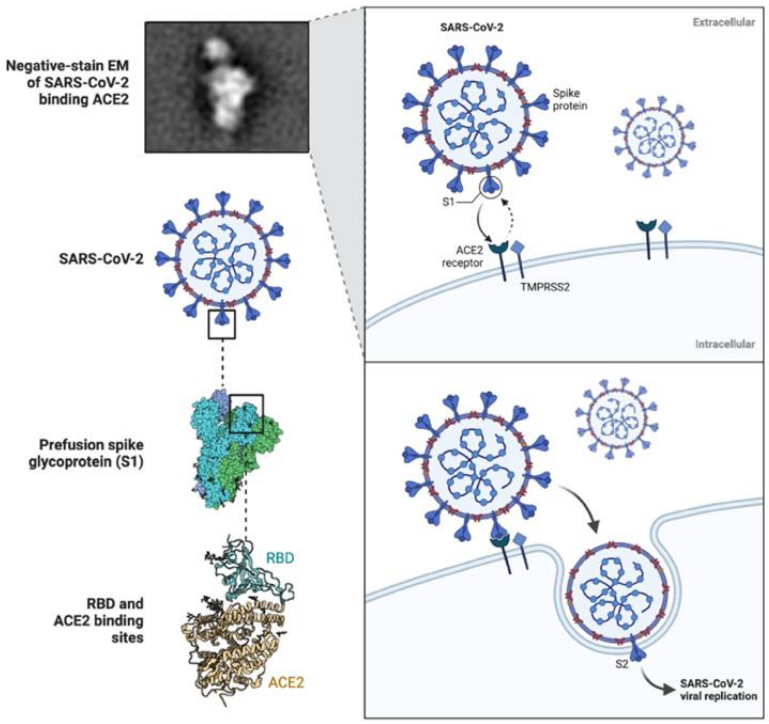

Figure 8 SARS-CoV-2 entry to the host cell by binding of the viral S protein to its receptor ACE2 on the cell membrane (6, 7)

In the alveoli, the virus infects alveolar epithelial cells, particularly AETII which express high levels of ACE2. Infection leads to significant damage to the alveolar epithelium, disrupting the structural integrity of the BAB (108-110). Infected cells and AMs release pro-inflammatory cytokines and chemokines which recruit immune cells to the site of infection. Although pulmonary capillary endothelial cells are not susceptible to SARS-CoV infections (111, 112), they are induced by the pro-inflammatory cytokines to express adhesion molecules like ICAM-1 and VCAM-1, facilitating neutrophil recruitment to the alveoli. Upon the activation of the neutrophils, they are guided by the chemokines to migrate through the endothelial layer. There they release reactive oxygen species (ROS) and proteases, which can further damage the BAB, increasing its permeability, allowing infiltration of fluid and recruitment of more immune cells into alveolar spaces, resulting in pulmonary edema

and impaired O_2 exchange (83, 108, 113, 114). In severe cases, this damage can lead to ARDS, a life-threatening condition characterized by widespread inflammation and rapid onset of respiratory failure (1, 115). The long-term consequences may include fibrosis and chronic lung disease, as the body attempts to repair the extensive damage (Figure 9) (115-117). The exact mechanism of progression from the infection to ARDS is not well understood, however, it is thought to involve several factors including the virus type, the infection severity, and the individual's immune response to the virus (118-121).

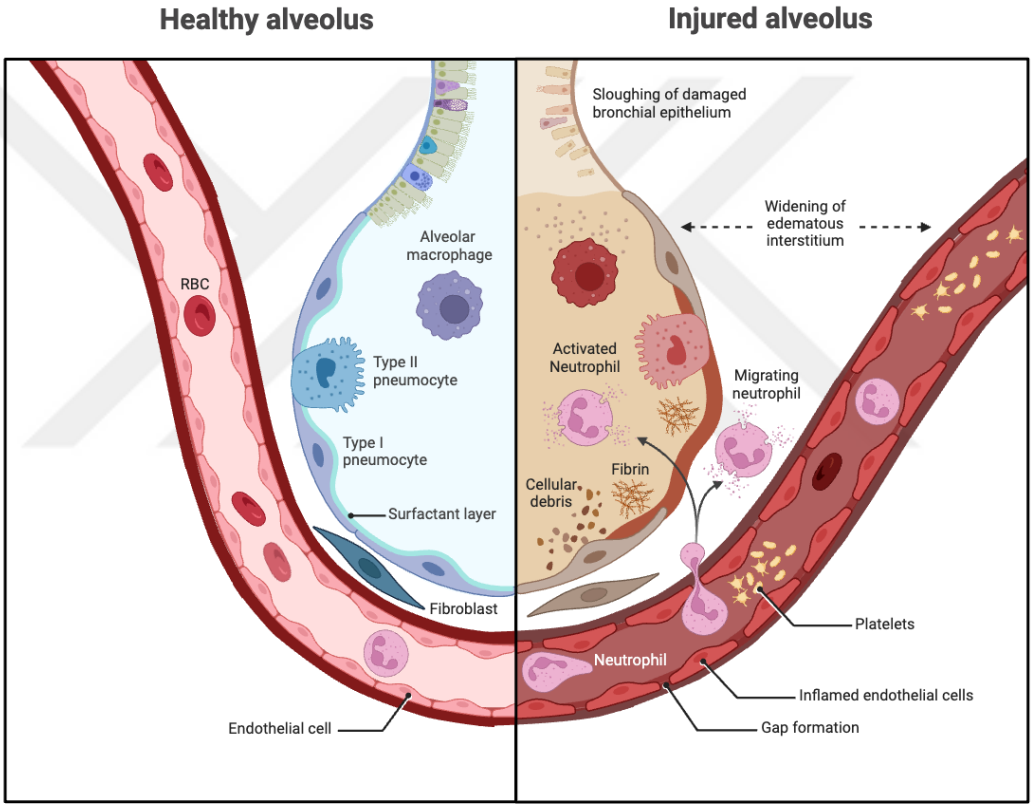

Figure 9 Changes in the alveoli in ARDS (1, 2)

2.4 The Use of the Model in Viral Infection Studies

The BAB model developed in this study serves multiple purposes in studying infection dynamics. It allows for the examination of viral infection within the alveolar space and at the cellular level, providing insights into the host's intrinsic response in ALI condition. In addition, the model allows studying the response given by the endothelium of the BAB which can become infected when the barrier is disrupted. Disruption of the barrier can trigger the expression of surface proteins on the endothelium, allowing immune cells in the bloodstream to anchor these sites (122). A significant feature of this model is its ability to closely mimic the native tissue microenvironment, including the composition and structure of the ECM. ECM components like collagen type I, fibronectin, and laminin significantly influence viral entry, replication, and host cell response. Changes in the ECM during infection can affect how the barrier responds, making it a crucial area of study for understanding the impact on barrier integrity and identifying potential therapeutic targets (5, 46, 123, 124). Furthermore, the model allows for studying gene expression changes in the host during viral infection while maintaining the 3D structure of the tissue which more accurately represents the native environment compared to traditional 2D models. It can reveal changes in cell signaling, immune responses, and metabolism that occur during infection, providing insights into the specific pathways involved (125-129). Key areas of study include:

- **Impact on Barrier Integrity:** Examination of how viral infections compromise the alveolar-capillary barrier, resulting in changes to intercellular junction proteins and increased permeability. The ECM's role in maintaining or disrupting barrier integrity is also crucial, as ECM remodeling can affect cellular responses to infection (5, 46, 123, 124). Analysis of the repair and regeneration processes of epithelial and endothelial layers can aid in the identification of potential therapeutic targets to enhance barrier recovery.

- **Drug tests:** Evaluation of the efficacy of drugs in preventing viral entry, replication, or spread within the BAB, as well as to test anti-inflammatory therapeutics aimed at preserving barrier integrity (127, 130-132).

- **Tracing the virus particles throughout the BAB:** Study of viral translocation across the barrier, enabling tracking of virus spread from the alveolar space to the bloodstream. Understanding these dynamics is key to studying how infections progress to systemic involvement. The model also allows for the inclusion of immune cells (133, 134).

- **Immune Evasion Strategies:** Investigation into how viruses modulate host immune responses, such as altering cytokine signaling pathways or reducing antigen presentation, to evade detection and clearance (135-137). Measurement of these molecules' release from infected cells to understand the inflammatory response and its role in disease severity, including the development of cytokine storms.

- **Transcriptional Changes:** Investigation of gene expression differences during viral infection in a 3D environment, providing a clearer picture of cellular events that may not be apparent in traditional models (52, 138). This includes identifying pathways involved in the host response and how they are influenced by the native tissue microenvironment. By the inclusion of AMs, the effect of environmental and lifestyle factors such as smoking or exposure to air pollutants can also be explored using this model. These conditions can influence the susceptibility of the alveolar barrier to viral infections and impact the immune response (139-142).

In this study, alveolar epithelial cells in the BAB model were infected with SARS-CoV-2 virus. Infection progression was monitored by measuring the production of new viral particles and measuring viral RNA levels. Barrier integrity was assessed using TEER measurements and immunofluorescence imaging of intercellular junction proteins. The potential infection of endothelial cells due to barrier disruption was also investigated. Overall, this model offers a comprehensive tool for studying the cellular

events during viral infections, including immune evasion, cytokine production, barrier integrity, ECM involvement, and gene expression changes. It serves as a valuable platform for drug testing, understanding the impact of environmental factors, and exploring personalized medicine approaches.

3 MATERIALS AND METHODS

3.1 Materials

PCL (poly(Ɛ-caprolactone), (MW: 50,000) was purchased from Polysciences (USA). Chloroform (#24216), gelatin (#G1890), triton X-100 (#T8787), quinacrine dihydrochloride (#Q3251), rhodamine B isothiocyanate labeled dextran (RITC-Dextran) (70 kDa) (#R9379), and thiazolyl blue tetrazolium bromide (#M2128) were obtained from Sigma Aldrich (USA). N,N-dimethylformamide (DMF) (#103053) was obtained from Merck Millipore (Germany). Fibronectin (#33016015), phosphate buffered saline (PBS) without Ca^{+2} and Mg^{+2} (#14190-094), Ham's F12 Nutrient Mixture (#31765-027), penicillin-streptomycin (#15140-122), DMEM without phenol red (#11054020) were purchased from Gibco (USA). CellTracker™ CMFDA Green dye (#C7025), TRIzol™ reagent (#15596026), GeneJet RNA Purification Kit (#K0731), and RevertAid First Strand cDNA Synthesis Kit (#K1622) were obtained from ThermoScientific (USA). Fetal bovine serum (FBS) (#04-007-1A) and bovine serum albumin (BSA) (#040071A) were purchased from Biological Industries (Israel). Laminin 511 (#LN511-0202) was obtained from Biolamina, Sweeden. Tough poly(lactic acid) (Tough PLA) filament (#RAL9003) was obtained from Ultimaker (Netherlands). Endothelial cell growth medium and supplements (#MD-0010) were purchased from ixCells, USA. PBS with Ca^{+2}, Mg^{+2} (#PBS-2A) was obtained from Capricorn (Germany). Fluorescein-sodium (0.4 kDa, #J61549) was purchased from Alfa Aesar (Germany).

The list of antibodies for immunofluorescence staining and their respective working concentrations used in this study are provided in Table 1.

Table 1 List of antibodies used for immunofluorescence staining studies

Antibody	**Brand/ Catalogue no.**	**Working concentration (v/v)**
Rabbit polyclonal Anti-Prosurfactant Protein C (SP-C) antibody, IgG	Abcam (ab90716)	1:400
Rabbit anti-Caveolin-1 antibody, IgG	Abcam (ab2910)	1:300
Mouse anti-Zonula Occludens 1 (ZO-1) monoclonal antibody	Invitrogen (ZO1-1A12)	1:100
Mouse anti-E-cadherin monoclonal antibody	ProteinTech (PTG 60335-1)	1:400
Mouse PE conjugated human anti-CD31 IgG1	BD Pharmingen (555446, Clone WM59)	1:10
Rabbit anti-VE-cadherin antibody	Abcam (ab33168)	1:400
Alexa Fluor™ 555 goat anti-mouse IgG	Invitrogen (A21424)	1:600
FITC-conjugated goat anti-mouse IgG	ProteinTech (SA00003-1)	1:100
CoraLite™ 488 goat anti-rabbit IgG	ProteinTech (SA00013-2)	1:500
SARS-CoV-2 Nucleocapsid Phosphoprotein polyclonal antibody	ProteinTech (28769-1-AP)	1:1000

3.2 Methods

3.2.1 Preparation of the mesh by electrospinning

In order to serve as the basement membrane of the BAB, an electrospun PCL mesh with randomly oriented nanofibers was produced. The fabricated mesh was characterized in terms of physical and mechanical properties. These properties were then optimized to serve the best basement membrane mimic for cellular attachment, proliferation, monolayer formation, and permeability to the passage of nutrients.

PCL (poly(ε-caprolactone) powder was dissolved (20% (w/v)) in a solution of chloroform : DMF with 70:30 (v/v) ratio. Polymer solutions were introduced to 10 mL syringes with a 21 G blunt tip needle, placed in a syringe pump (New Era Pump Systems Inc., USA), and connected to a power supply (Gamma High Voltage Res., USA). A grounded aluminum plate (20 x 20 cm^2) covered with a sheet of Al foil served as the collector (Figure 10). Electrospinning conditions were optimized to obtain fibers with nano thickness. Fabrication conditions were: flow rate: 0.4 mL/h, distance (between the injector tip and collector): 15 cm, and power: 20 kV at RT. The duration of the spinning was optimized to 3 min.

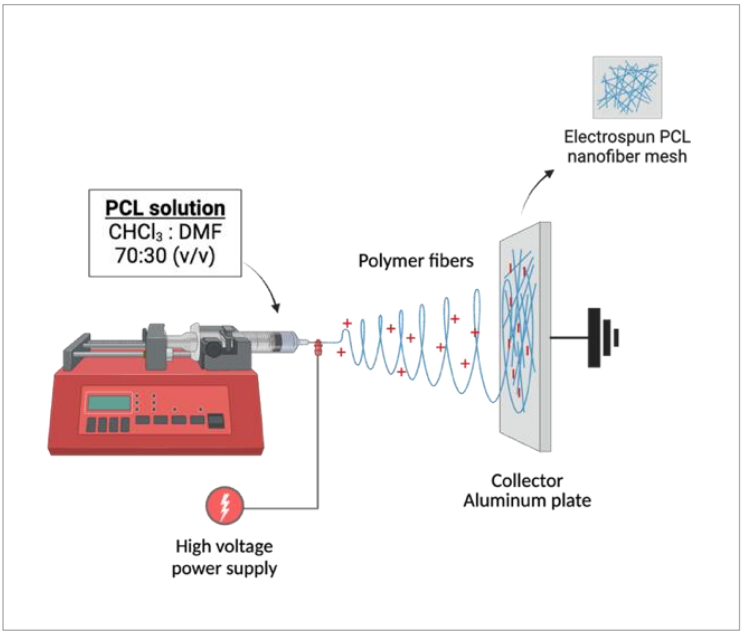

Figure 10 Illustration of the electrospinning setup

3.2.2 Characterization of the mesh

3.2.2.1 Fiber thickness, mesh thickness, and pore size

Scanning electron microscopy (SEM) (Zeiss EVO 10, Germany) was used to determine the properties of the mesh after coating with Au/Pd. Fiber thickness, mesh thickness, and pore size were calculated using NIH Image J Software (version 1.53t) (143) using the SEM micrographs.

3.2.2.2 Surface hydrophilicity determination

The surface hydrophilicity of the mesh was assessed through water contact angle (WCA) measurements, employing the Sessile Drop method on pristine and protein coated meshes, and a thin film of PCL produced by solvent casting to measure the WCA. Water droplets (2 μL) were placed onto the samples, and the contact angle was measured after 5 s with a goniometer (DS25E Drop Shape Analyzer, Krüss, Germany), utilizing Krüss Advance software (v1.10). Measurements were conducted at 3 distinct positions on each sample, with 3 different samples utilized for the assessment. The mean contact angles were determined by averaging the right and left side contact angles. Data was presented as the mean ± standard deviation.

3.2.2.3 Mechanical testing

A uniaxial tensile test was conducted using mechanical tester (Shimadzu, Autograph ASG-X, Japan) to measure the stiffness of the meshes. Samples with 20 mm height x 10 mm width, and 40 μm thickness were clamped at both ends, and a tensile load was applied at a rate of 5 mm/min using a 20 N load cell (n=5). Young's Modulus (*E*) was calculated from the slope of the initial linear portion of the stress-strain curves (Figure 11) within the 10% linear strain region (Equation 1). The maximum values obtained with each curve constituted the ultimate tensile stress (UTS). Results were presented as the mean ± standard deviation.

$$E = \sigma / \varepsilon \quad (1)$$

where

σ: Stress (MPa, N/mm^2)

ε: Strain (mm), Deformation (%)

E: Young's modulus

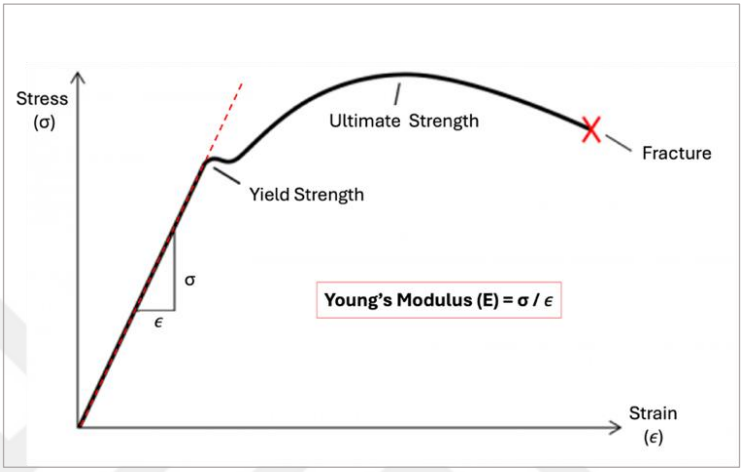

Figure 11 Stress-strain curve

3.2.2.4 Cytotoxicity test

Although PCL is approved by the FDA as biocompatible, MTT cell viability assay was still conducted to confirm that the electrospun PCL meshes do not exert any toxic effect on cells. For this purpose, ISO 10993 – 5, "Tests for *in vitro* cytotoxicity" standard was followed. PCL meshes were fabricated and sterilized as described in section 3.2.1. Then, they were immersed in cell culture medium in a cell culture plate with a surface area to medium volume ratio of 3-6 cm^2/mL, and incubated for 72 h (37°C, 5% CO_2). The culture media were collected and stored at 4ºC. A549 cells (number was determined with Thoma slide) were seeded in a 96 well plate (p31, $1x10^4$ cells/well). The media of PCL meshes and pristine culture medium were added to the well plates with cells. After 24 h of incubation (37°C, 5% CO_2), cell viability was assessed by MTT assay by applying thiazolyl blue tetrazolium bromide solution (150 µL of 10% (v/v) 5 mg/mL) in DMEM without phenol red to each well. After 4 h of incubation (37°C, 5% CO_2), formazan precipitates, formed by the reduction of the

tetrazolium salts by cellular reductases, were dissolved with 200 µL DMSO. The absorbances at 570 and 630 nm were measured using a Microplate Reader (Victor Nivo 5T, Perkin Elmer USA). The absorbance values at 630 nm and the average absorbance value of the blank sample (DMEM) were subtracted from the 570 nm values. Cell viability was presented as percent viability relative to the negative control.

3.2.3 Construction of the model

The construction of the model began with placing the mesh to cell culture inserts, serving as a scaffold for co-culture and enabling the separation of apical and basal compartments. PCL meshes were collected using optimized electrospinning conditions, then were placed in a vacuum oven overnight to remove any residual solvent. To detach the meshes from the foil surface, incisions were made with a blade (ca. 1 cm^2 in size), and the meshes were gently peeled off from the surface ensuring each piece was handled without stretching. The inserts were designed using Sketchup Software and 3D printed (Ultimaker, Netherlands), sterilized in 70% EtOH for 1 h, then the meshes were placed to the inserts and secured by rings (Figure 12). The surface area of the meshes for cell growth was calculated as 0.43 cm^2.

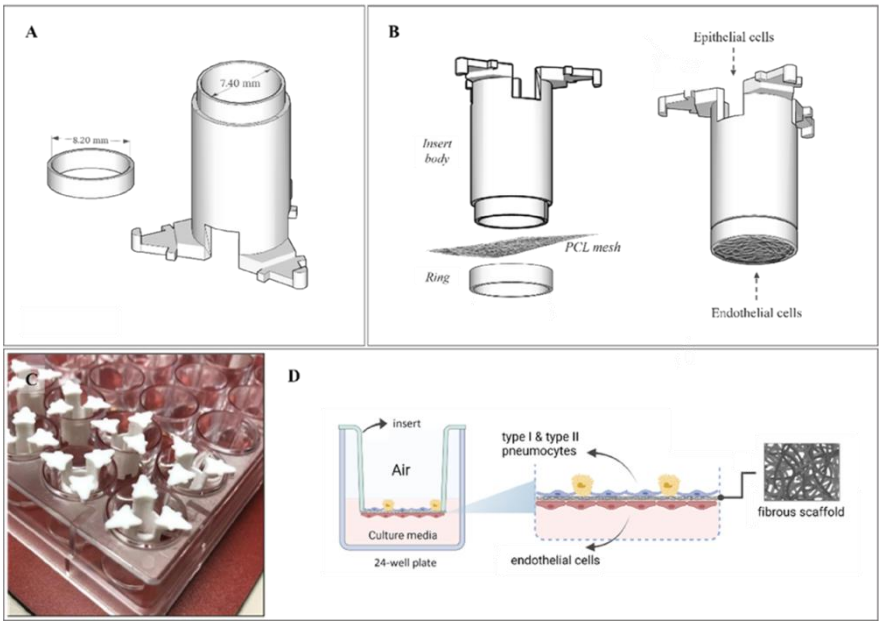

Figure 12 The cell culture insert and placement of the mesh to serve as the scaffold for co-culture of the cells. A) The insert body and ring, B) Mesh placement to the insert, C) Inserts placed in a 24-well plate, D) Illustration of the co-culture.

Both sides of the meshes were exposed to UV light for 30 min each in a biosafety level 2 (BSL-2) cabinet. Meshes were then treated with O_2 plasma (30 W, 6 s) (Diener Pico, Germany), and coated with a 75 µl of protein solution within 5 min after the treatment. The protein composition was optimized to ensure that the cells did not penetrate to the other side of the mesh and were grown as separate monolayers on both sides while facilitating the cobblestone morphology of pHUVEC cells. Meshes were coated with either a mixture of fibronectin (10 µg/cm^2), laminin 511 (0.5 µg/cm^2), and collagen type I (10 µg/cm^2) (37°C for 2 h), or gelatin (0.5%) in the place of collagen type I. pHUVECs were stained with CellTracker™ CMFDA Green dye before cell seeding (10 µM, 1 h at 37°C, 5% CO_2), then their spreading was imaged by fluorescence microscope using tiles scan mode (Zeiss Axio Imager M2, Germany) on Day 2 after seeding. Monolayer formation by the A549 cells was assessed through IF staining of ZO-1 and imaged using CLSM z-stack imaging. The meshes were coated with the determined protein mixture, then were air-dried overnight in the cabinet. The next day, suspension of pHUVECs (p3, 2x10^4 cells/cm^2) was applied to the bottom side of the meshes. After incubation for 1.5 h to allow cell attachment to the mesh surface (37°C, 5% CO_2), they were inverted back into a 24-well plate containing 500 µL of the co-culture medium. The following day, A549 cells (p29, 1x10^4 cells/cm^2) were seeded on the top side of the mesh. Cells were expanded for 3 days in co-culture under submerged conditions (37°C, 5% CO_2) (Figure 13).

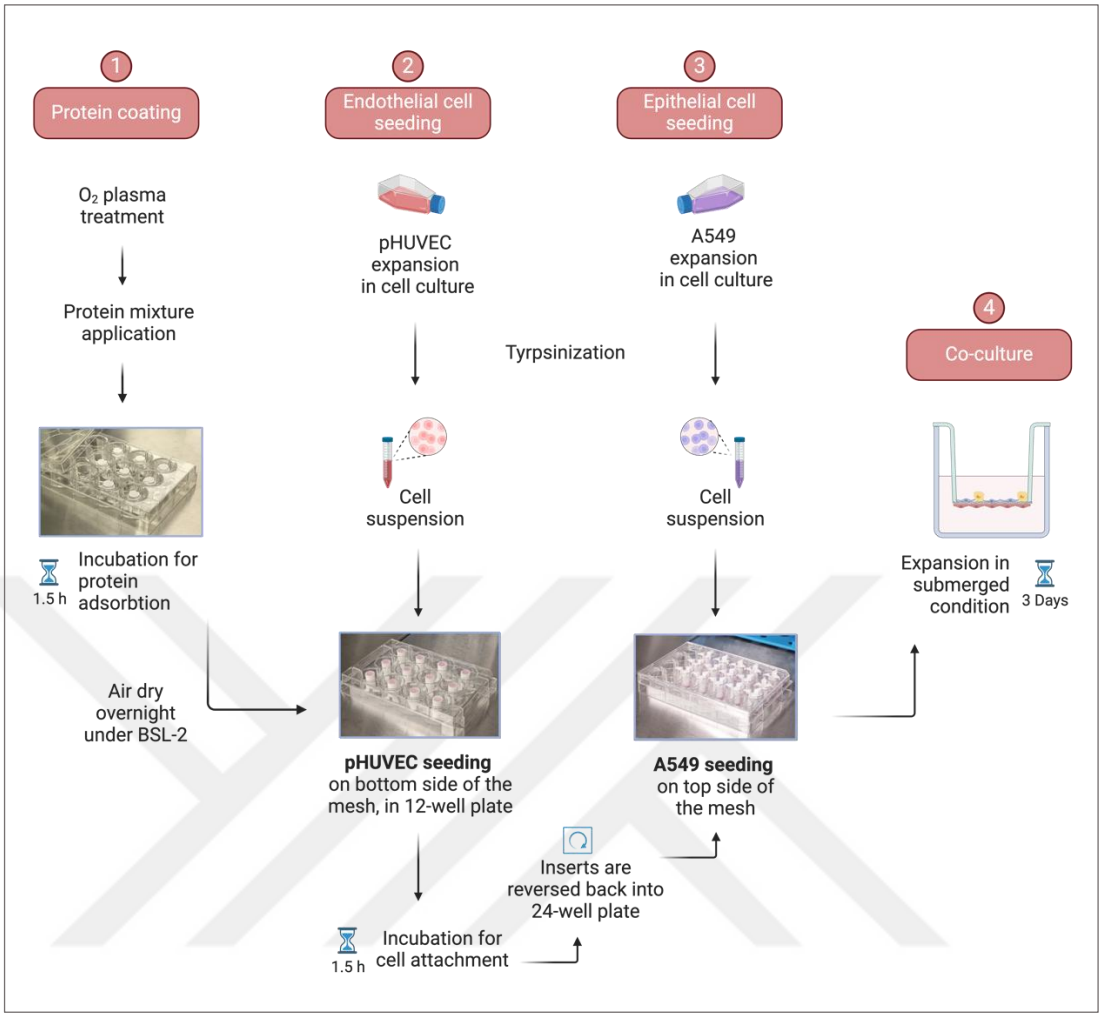

Figure 13 Overview of the steps to construct the barrier model.

On Day 4 after seeding, the culture was transitioned to air-liquid interface (ALI) condition by removing the media from the top side of the mesh to allow A549 cells to be in contact with air. The cells were kept in ALI condition until Day 14 (37°C, 5% CO_2) (Figure 14). Media was refreshed every day after a gentle wash of the cells with warm PBS with Ca^{+2} and Mg^{+2}.

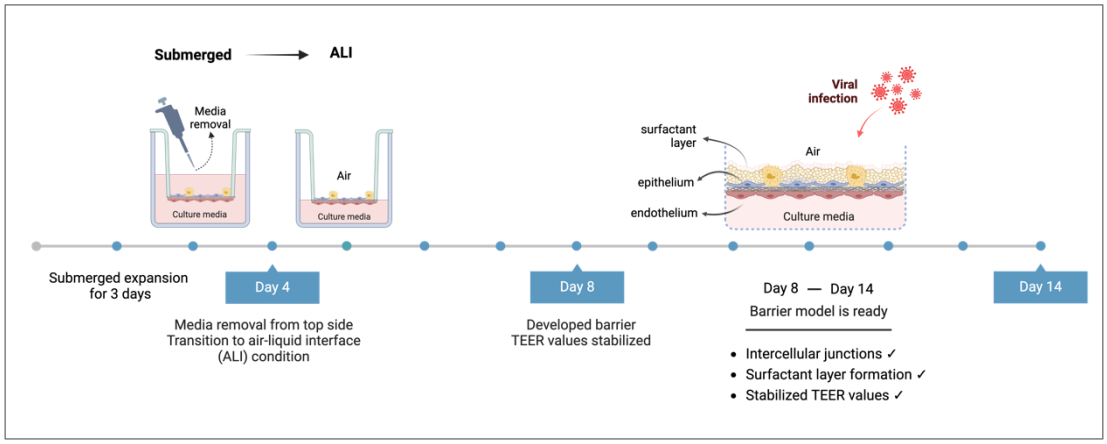

Figure 14 Model preparation and use timeline

Primary human umbilical vein endothelial cells (pHUVECs) were a kind gift of Prof. Halime Kenar (Appendix-1, Ethical committee approval). These cells were cultured on 0.5% gelatin coated tissue culture treated plates (TCP) with a serum free chemically defined Endothelial Cell Growth Medium containing supplements and penicillin-streptomycin (0.1%). **Adenocarcinomic human alveolar basal epithelial cells (A549)** were kindly provided by Dr. Rengin Reis (Faculty of Pharmacy, ACU). The cells were cultured on TCP with Ham's F12 medium with 10% FBS and 1% penicillin-streptomycin ("Ham's F12 complete"). Media was changed every 2 days following a gentle wash of the cell monolayer with warm PBS. The cells were expanded for 4 days (37°C in 5% CO_2) until they reached confluence. Morphologic evaluation and imaging of the cells was conducted using an inverted microscope in bright field mode (Zeiss Primovert, Germany).

In order to determine the optimum culture medium composition suitable for the co-culture of both cell types, cell viability was determined with various media mixtures over a period of 7 days using MTT assay. pHUVECs (p4, $2.5x10^3$ cells/well) and A549 cells (p29, $2.5x10^3$ cells/well) were seeded in 96 well plates with their respective endothelial and epithelial media (Day 0). The next day, the following media were applied to the cells (n=3):

- Endothelial medium (ixCells medium)
- Endothelial: Epithelial (1:1) medium mixture

- Endothelial: Epithelial (3:1) medium mixture
- Endothelial: Epithelial (1:3) medium mixture
- Epithelial medium (Ham's F12 complete)

Cell viability (%) was assessed for Day 0 (3h after the cell seeding), Days 1, 3, 5, and 7 by MTT assay, as described previously (Section 3.2.2.4). Data was analyzed to determine the media composition providing the highest cell viability for both cell types. All groups were studied in triplicates except Day 0 (n=9).

3.2.4 Characterization of the model

The model was tested in terms of the expression of the cellular phenotypic markers on the basement membrane by the seeded cells, the presence of a barrier with a monolayer of the cells forming intercellular junctions, and the existence of barrier integrity. The tools to use at this step include immunofluorescence staining of the phenotypic markers and intercellular junction proteins, determining the trans-epithelial electrical resistance (TEER) and the permeability of the barrier against representative (Fluorescein, 0.4 kDa) and large (RITC-Dextran, 70 kDa) molecules, differentiation of alveolar epithelial type II cells into type I cells at ALI condition, and determination of the presence of a surfactant layer.

3.2.4.1 Transepithelial electrical resistance measurement

TEER measurements were conducted using EVOM3 Epithelial Volt/Ohm Meter equipped with STX4 electrodes (WPI, Germany) (Figure 15). First, the electrodes were validated following the manufacturer's protocol in which the resistance was measured using a series of KCl solutions in dH_2O (10, 20, 40, 80, and 160 mM). The measurement procedure was designed to minimize possible variations in environmental factors, such as temperature and pH, as well as the height of the liquid in the well plate which potentially affect the results. This was achieved by replacing the co-culture media (37 ºC) with 1600 µL PBS (with Ca^{+2} and Mg^{+2}) at RT to avoid temperature and pH variations. Then the samples were allowed to adapt for 3 min until

the liquid level was stable. Individual cultures of A549 cells (n=6) and pHUVEC cells (n=6) on mesh, and their co-culture (n=15) were used for the measurement. The mean resistance measured for the inserts with protein coated meshes was determined as the blank (n=3). Resistance across the meshes was recorded every 2-3 days until a plateau was reached. The values were then used to calculate TEER (Ω·cm²) using Equation 3:

$$\text{TEER } (\Omega \cdot \text{cm}^2) = \text{Resistance } (\Omega) \text{ x Area of the Mesh } (\text{cm}^2) \quad (3)$$

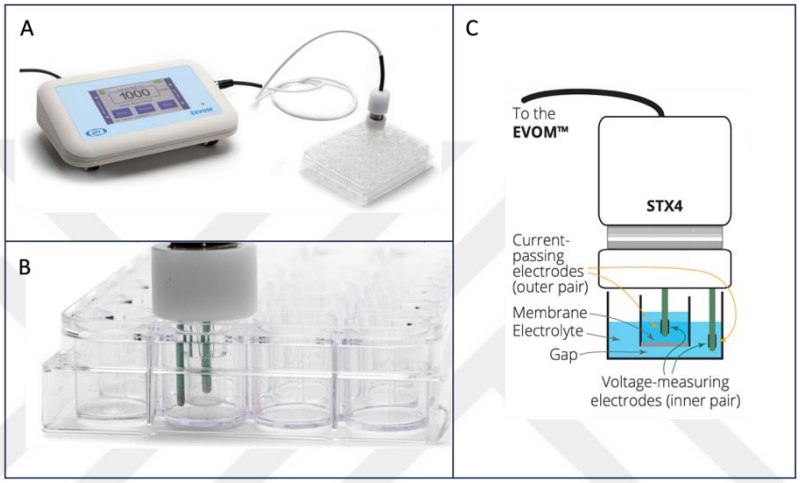

Figure 15 TEER device components and the working principle. A) EVOM ohmmeter device with STX4 electrodes, B) Electrodes placed in a 24 well plate, C) Components and the working principle of the STX4 electrodes.

3.2.4.2 Permeability tests

The permeability of the barrier to molecules of different sizes was determined using fluorescein sodium (0.4 kDa) and RITC-Dextran (70 kDa). The electrospun PCL meshes that were prepared for the permeability tests were pristine, protein coated, and seeded with cells on both surfaces. The meshes attached to inserts were placed in a 24 well plate containing 950 µL PBS (with Ca^{+2} and Mg^{+2}). The samples were then allowed to adapt for 3 min until the liquid level was stable. Then, 50 µL of 5 µg/mL fluorescein sodium and 5 mg/mL RITC-Dextran solutions in PBS were separately added on the meshes. Samples were incubated (37°C, 5% CO_2), allowing the diffusion of the molecules through the meshes. At 20, 40, 60, and 120 min, the liquid in the lower compartment was mixed by pipetting to ensure homogeneity of the particles in

the media. 10 µL sample was taken from the lower compartment, diluted to 200 µL in a black 96 well plate, and the relative fluorescence intensity (RFU) was measured using a multimode plate reader (Victor Nivo, Perkin Elmer, USA) at λ_{ex}: 480, λ_{em}: 530 for fluorescein, and λ_{ex}: 560, λ_{em}: 585 for RITC-Dextran (Figure 16).

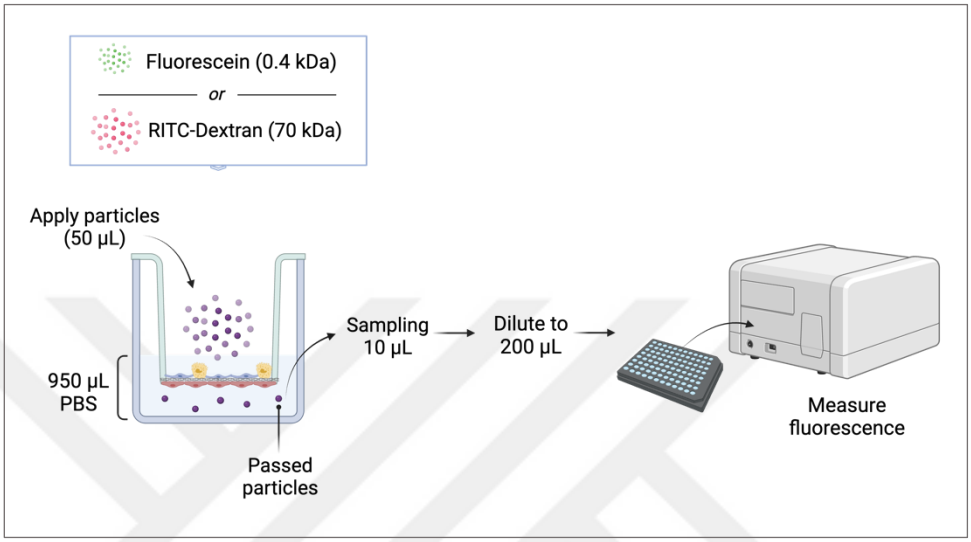

Figure 16 Schematic representation of the permeability testing procedure

The transfer of the molecules through the meshes over time (mass transport, %) and the apparent permeability (P_{app}) were calculated. The apparent permeability (P_{app}) was calculated using Equation 4:

$$P_{app} = \frac{dQ}{dt} \times \frac{1}{AC_0} \quad (4)$$

where

dQ/dt is the amount of product present in the acceptor side (basal compartment) as a function of time (µmol/s),

A is the area of mesh (cm^2),

C_0 is the initial concentration of product applied in the donor side (apical compartment) (µM).

An exemplary calculation for the barrier model's apparent permeability (cm/s) at 120 min:

- The applied concentration of fluorescein: 5 µg/mL (in 50 µL PBS);
- Applied amount of fluorescein: 0.25 µg
- Amount of fluorescein passed to basal side at 120 min: 0.01895 µg

$$Papp = \frac{0.10183\mu g/1000\mu l}{60 * 120\ s} * \frac{1}{0.43\ cm^2 * 5\mu g/1000\mu l}$$

$$Papp = 3.95E\text{-}05\ cm^2$$

3.2.4.3 Immunofluorescence staining of the junction proteins

A549 cells were grown on the meshes for 7 days until confluence, then fixed with 4% PFA for 20 min. Cells were then permeabilized with triton X-100 for 10 min at RT. After triple wash with PBS with Ca^{+2}, Mg^{+2} for 5 min, 3% BSA was added and incubated for 30 min to block non-specific protein binding. Primary antibodies targeting Caveolin-1 (AETI phenotypic marker) and Prosurfactant Protein C (SP-C) (AETII phenotypic marker), were applied and incubated overnight at 4°C. Following the removal of primary antibodies and triple wash with PBS with Ca^{+2}, Mg^{+2}, secondary antibodies were added and incubated at 37°C for 1 h. After an additional triple wash, DAPI staining for cell nuclei was conducted for 10 min. The same procedure was performed with pHUVECs to test the expression of endothelial cell marker CD31 (Platelet/endothelial cell adhesion molecule-1 (PECAM-1) and Vascular Endothelial Cadherin (VE-Cadherin) adherence junction protein. Imaging was performed with a confocal laser scanning microscope (CLSM) (Zeiss LSM900, Germany). The list of antibodies used in the study were listed in Table 1.

3.2.4.4 Imaging of lamellar bodies and surfactant layer

In order to confirm the presence of lamellar bodies in A549 cells, fluorescent dye quinacrine dihydrochloride which has a high affinity for phospholipids, was used. A549 cells (p29) grown to confluence on TCPs were fixed with 4% PFA for 20 min. Then, quinacrine dihydrochloride solution (10 μM) was added to the cells and incubated for 1 min at RT. After triple washing with PBS, DAPI was applied to stain cell nuclei. Imaging was performed with confocal microscopy at 40X magnification (λ_{ex}: 436, λ_{em}: 525 nm).

Statistical Analyses

a) SEM Image Analysis

SEM images of meshes were analyzed for their fiber diameter, mesh thickness, and pore area using ImageJ software (version 1.53t) (143). Average fiber diameter was determined by measuring 20 randomly selected fibers from 3 different images (5,000X). The average mesh thickness was determined by measuring 10 positions from the side view images. The entire process, including fabrication conditions, SEM imaging, and analysis, was repeated for a minimum of three times. Data was presented as the mean ± standard deviation.

b) MTT assay for cytotoxicity and co-culture medium optimization tests

Each condition was tested with 9 samples. Cell viability (%) values were normalized to the initial viability values obtained on Day 0 (3 h after cell seeding). Sample groups were analyzed with two-tailed t-test using Python programming language, assuming equal variances where the null hypothesis is the two population means are equal. For comparison of significant differences between groups, the cut off p value was set as 0.05. Data was presented as mean ± standard deviation.

c) TEER measurements

All TEER measurements were repeated three times for each sample, and the measurement was repeated with different sample sets for a minimum of three times. Data was plotted on a line chart as a function of time (Days) and presented as the mean ± standard deviation. Statistical analyses for the other tests are explained in their corresponding sections in the Methods.

3.2.5 Testing the model for use in viral infection studies

In order to test the developed BAB model for use in viral infection studies, SARS-CoV-2 was used as a representative virus infecting the alveolar epithelial cells. The infection was performed in the Biosafety Level 3 (BSL-3) facility of Ankara University Faculty of Veterinary Medicine, Department of Virology, using SARS-CoV-2 Ank1 isolate (GenBank Accession. No: MT478018) which was isolated, sequenced, and reported by Hanifehnezhad et al., 2020. Official permissions for the sample collection and viral propagation were previously provided by the authors (144).

The infection was performed on the barrier models on Day 12 after cell seeding and at ALI condition (n=15). Virus suspension was applied from the top side directly on the epithelium at a multiplicity of inoculation (MOI)=1, except for the uninoculated control groups (n=6) treated with co-culture media. The samples were incubated for 30 min (37 °C, 5% CO_2), then the inoculation medium was collected and kept at -80 °C to determine the initial number of infectious particles (viral titer) (plaque-forming units, pfu/mL) that interacted with the cells through plaque assay as described previously (144). Media was refreshed at 24, 48, and 72 hours post inoculation (hpi), and collected media were stored at -80°C for viral RNA isolation. At 72 hpi, TEER measurement was performed with all samples, then either fixed with 4% PFA for IF staining (n=6) or stored at -80 °C after Trizol application for total RNA isolation. IF staining was performed as described in Section 3.2.4.3 for the viral Nucleocapsid (N) protein and ZO-1.

4 RESULTS

The key characteristics of the electrospun basement membrane mimic, such as fiber thickness, pore size, hydrophilicity, and stiffness (Young's Modulus), were evaluated to ensure that it closely replicates the natural pulmonary basement membrane. A viable and anatomically correct barrier model was produced by optimization of the scaffold surface for appropriate cell attachment, formation of cellular monolayers on opposite sides of the mesh, optimization of the co-culture media composition, and the surfactant layer production under ALI condition. Functionality of the model was assessed by the imaging of the intercellular junction proteins, measurement of transepithelial electrical resistance (TEER), and testing permeability of the model membrane to molecules of different sizes. Finally, the functionality of the model for use in viral infection studies was evaluated by monitoring the effects of SARS-CoV-2 infection.

4.1 Characteristics of the Mesh

4.1.1 Fiber thickness, mesh thickness, and pore size

The fiber diameter and pore size of the mesh were determined using SEM images using NIH FIJI (Image J 1.53t) (143). The fiber diameter was found to be 100-600 nm. The pore area was 0.104 μm^2, and the mesh had 17% porosity and a mean pore diameter of 2.46±0.57 μm. The resulting nanofibrous mesh produced had a thickness of less than 20 μm, with interconnected pores (Figure 17).

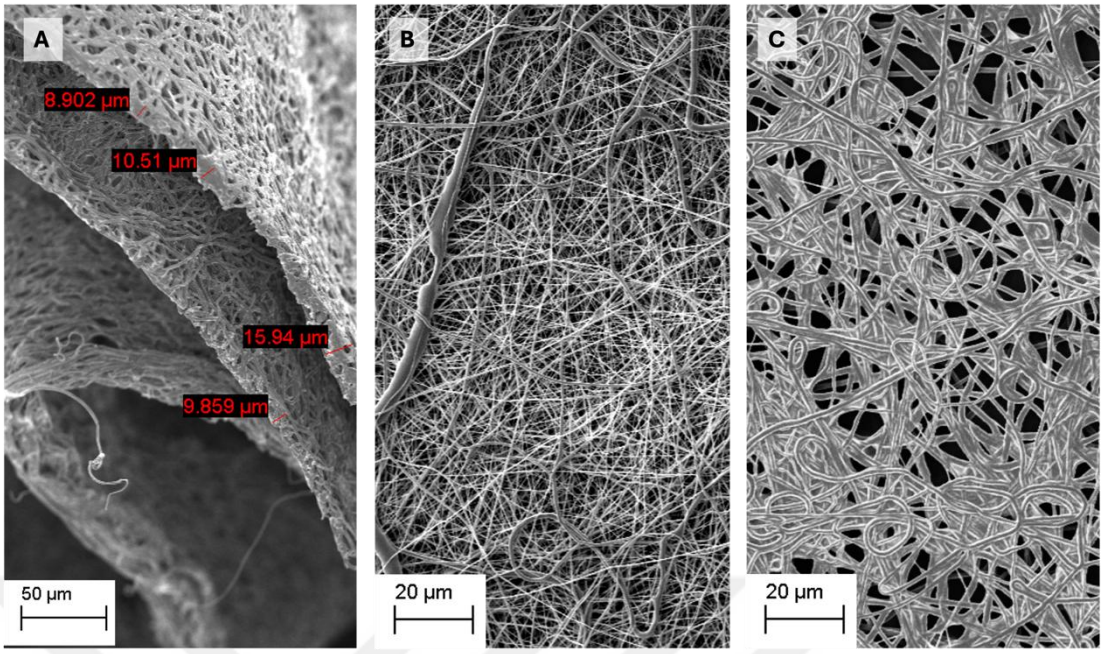

Figure 17 SEM micrographs of electrospun PCL meshes. A) Cross section, scale bar: 50 µm, B) Front surface, C) Back surface (facing the collector). Scale bar: 20 µm.

4.1.2 Surface hydrophilicity

Water contact angle values obtained for the PCL film, the pristine and protein coated mesh samples, and representative images of the measurements are presented in Figure 18. It can be seen that PCL is hydrophobic and appears to get more hydrophobic when it becomes a mesh. This is due to the water droplet being unable to make contact with a surface due to the presence of gaps as a result of being in contact with a discontinuous surface such as a mesh. The front surface of the mesh was more hydrophobic compared to the back surface facing the collector, which was Al foil coated with polyethylene glycol (5% in EtOH) to facilitate the detachment of the meshes from the foil surface. Upon protein coating the mesh becomes more hydrophilic but is still on the hydrophobic side (ca. 94°), not like the best surfaces for the cells to attach to (around 60°). However, a moderate hydrophobicity was necessary to maintain pHUVEC cell suspension in a droplet form on the mesh surface, allowing for cell attachment during the incubation period.

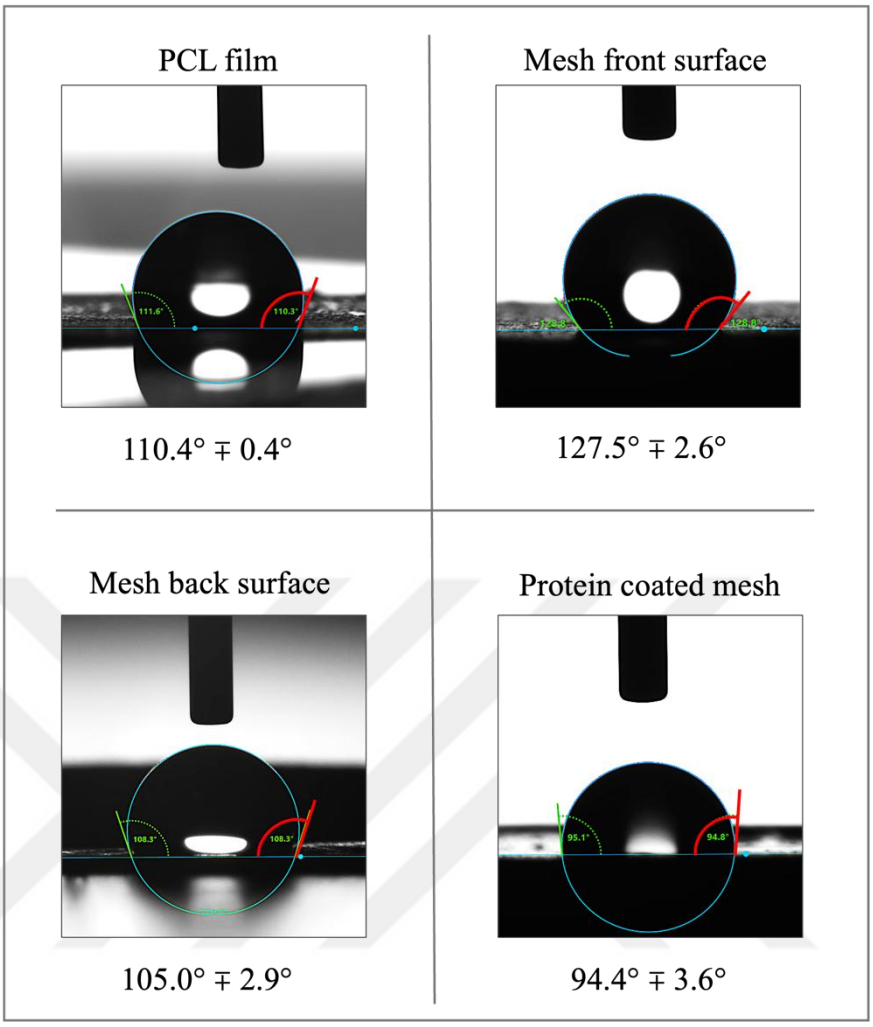

Figure 18 Water contact angles of untreated PCL film and meshes, and protein coated mesh.

4.1.3 Mechanical properties

The stress–strain plots obtained by tensile testing of PCL meshes is presented in Figure 19. The Young's Modulus of the meshes was determined by measuring the slope of initial linear elastic region. The slope (Young's Modulus) was calculated as 8.07 ± 0.81 MPa while the ultimate tensile stress (UTS) was determined as 1.63 ± 0.26 MPa.

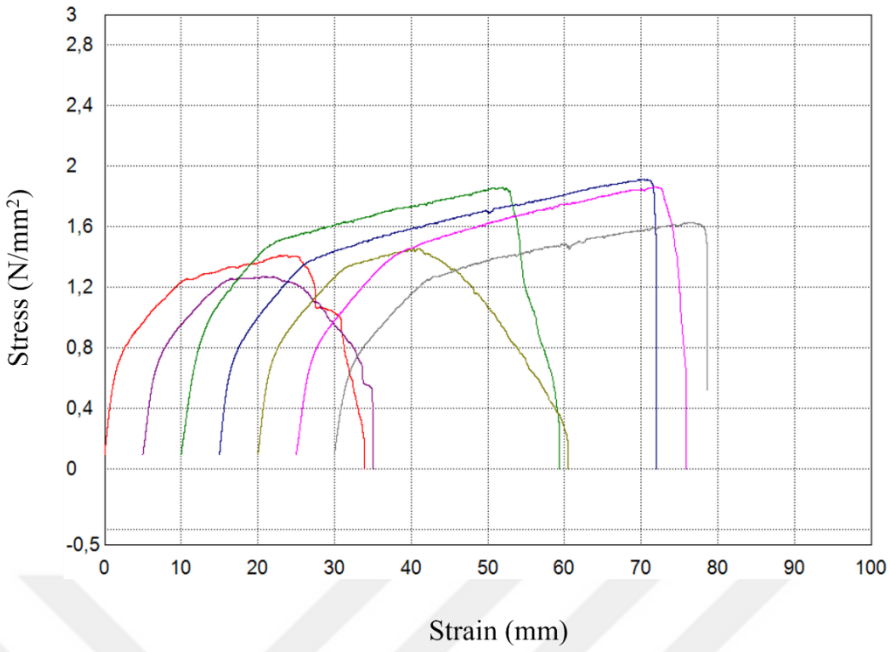

Figure 19 Stress-strain curve of the electrospun PCL meshes

The stiffness of the native barrier has been reported to be in the range of kPa (33, 145), therefore, the modulus of the mesh used in the model is about ten times that of the native tissue. However, the overall stiffness of the basement membrane mimic is not solely due to the mesh, as it is coated with collagen type I, which provides additional strength and elasticity. During breathing, the barrier tissue undergoes approximately 10% extension due to cyclic inhalation and exhalation movements (33, 146). The stress-strain curve indicates that the mesh remains in the elastic region within this 10% displacement.

4.2 Characteristics of the Model

4.2.1 Cell attachment and monolayer formation

During the optimization of the protein mixture composition for optimum cell attachment, the use of gelatin instead of collagen type I was tested as gelatin had been used to attach the cells to tissue culture flasks. However, the presence of gelatin led to the formation of multilayers of endothelial cells possibly caused by the relatively thick gel environment that allowed the cells to penetrate various layers (Figure 20A). Using

a lower gelatin concentration may have solved this problem, however, collagen type I was essential due to both its abundance in the native barrier, contributing structural strength, and in biological signaling through interaction with fibronectin and laminin. When seeded on the collagen type I – fibronectin – laminin mixture, pHUVECs created a monolayer of cells without penetrating to the opposite side and showed cobblestone morphology which is observed when they form a monolayer and reach contact inhibition with full confluency, typically under conditions that mimic the vascular endothelium (Figure 20B).

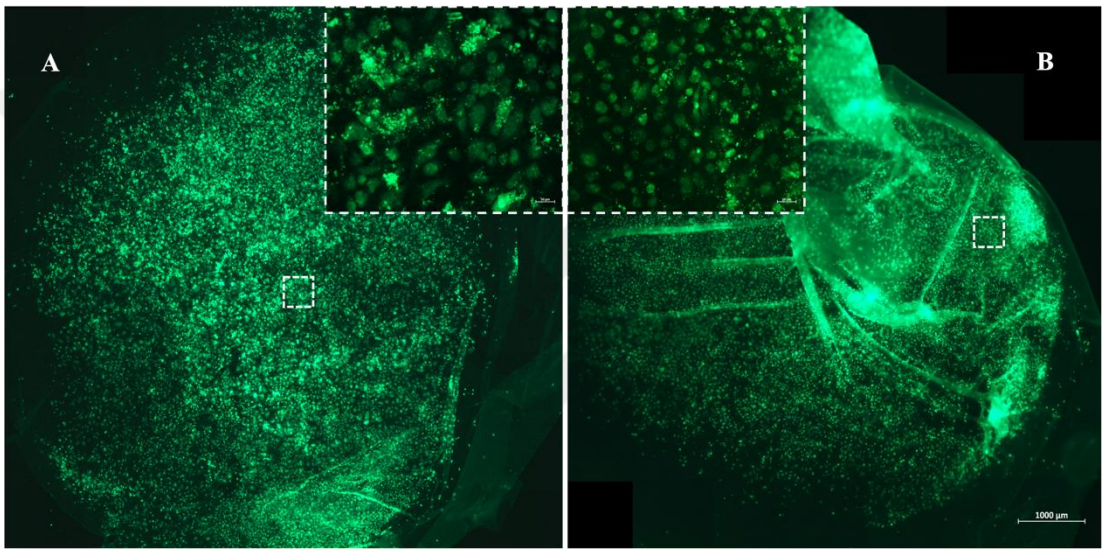

Figure 20 Fluorescence micrographs of pHUVECs (labeled with CellTracker™ Green) grown for 2 days on protein coated meshes. A) Collagen type I-fibronectin-laminin mixture, B) Gelatin-fibronectin-laminin mixture. Whole meshes were imaged using tiles at 10X magnification, and then stitched together (Scale bar: 1000 µm). Marked regions (dashed with white squares) were individually captured to serve as representative areas illustrating the overall cell morphology across the surfaces (Scale bar: 50 µm).

Both epithelial and endothelial cells attached to the mesh surface coated with the defined protein mixture, without penetrating through to the opposite side when seeded separately (Figure 21, Figure 22). Location of the signal given by the cells was observed to be in the range of 0 - 5 µm thickness on the mesh surface (Figure 21C, Figure 22D).

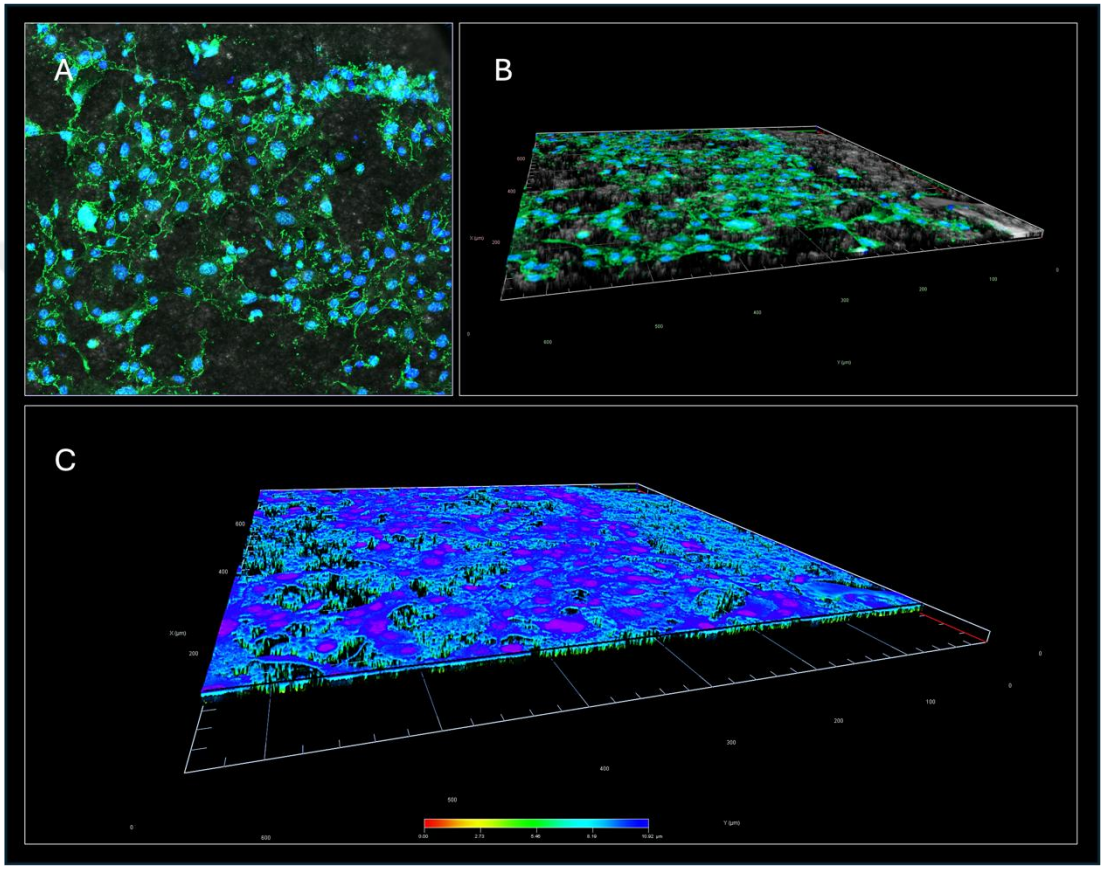

Figure 21 CLSM micrographs of pHUVECs grown on meshes for 5 days, IF stained with VE-Cadherin (green). A) Top view. Scale bar: 20 µm, B) z-stack top view; signal obtained from the mesh (gray), C) z-stack top view; depth level of the obtained signal scaled by color scale (µm). Nuclei stain: DAPI (blue).

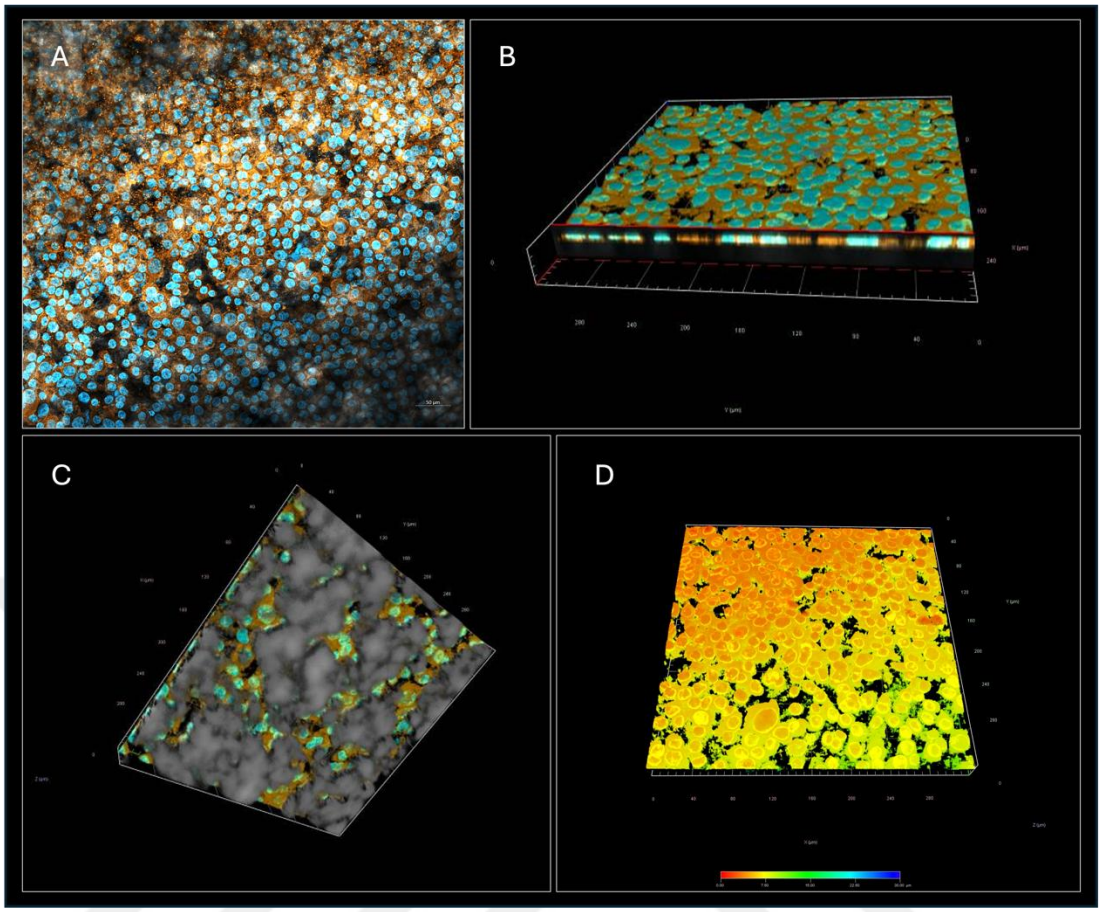

Figure 22 CLSM micrographs of A549 cells grown on meshes for 5 days, IF stained with ZO-1 (orange). A) Top view. Scale bar: 50 µm, B) z-stack top view and z-axis cross section, C) z-stack bottom view; signal obtained from mesh (gray), D) z-stack top view; depth level of the obtained signal scaled by color scale (µm). Nuclei stain: DAPI (turquoise)

The morphology of the cells grown on TCP and protein coated meshes was studied through bright field and SEM microscopies, respectively. pHUVECs at passage 3 (p3) grown on TCP displayed their characteristic flat, polygonal, or slightly elongated shape, forming a packed monolayer typical of the cobblestone morphology of endothelial cells (Figure 23A). Cells grown on the meshes showed a similar morphology in the linear plane but with prominent surface roughness due to the wrapping of their cytoplasm around individual fibers within the mesh (Figure 23 C-D). This wrapping suggests strong adherence, potentially enhancing cellular stability and interaction with the basement membrane mimic, which is essential for constructing complex 3D models. During the fixation process cells partially detached from each other, stretching intercellular junctions both on TCP and on meshes (Figure 23 B-D).

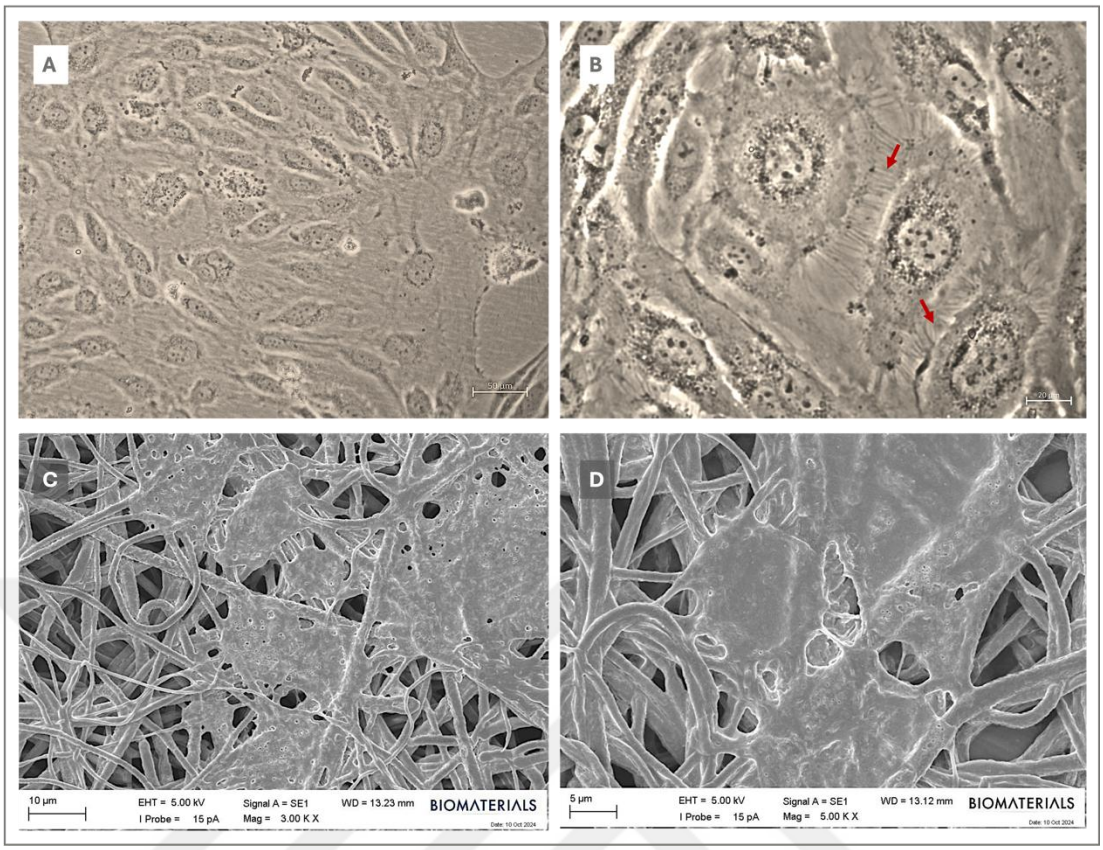

Figure 23 pHUVECs grown on TCP and protein coated meshes. Bright field micrographs on TCP A) Under normal culture conditions, B) After fixation, showing stretched intercellular junctions (red arrows). C-D) SEM micrographs of the cells on meshes with different magnifications. Scale bars were separately indicated on each image.

A549 cells (p29) grown on TCP displayed the morphology of a mixed population of AETI and AETII cells with the characteristic flattened squamous morphology and the rounded spherical form, respectively (Figure 24 A-B). Similar to pHUVECs grown on mesh, A549 cells showed a prominent surface roughness due to the wrapping of cytoplasm around individual fibers within the mesh (Figure 24 C-D).

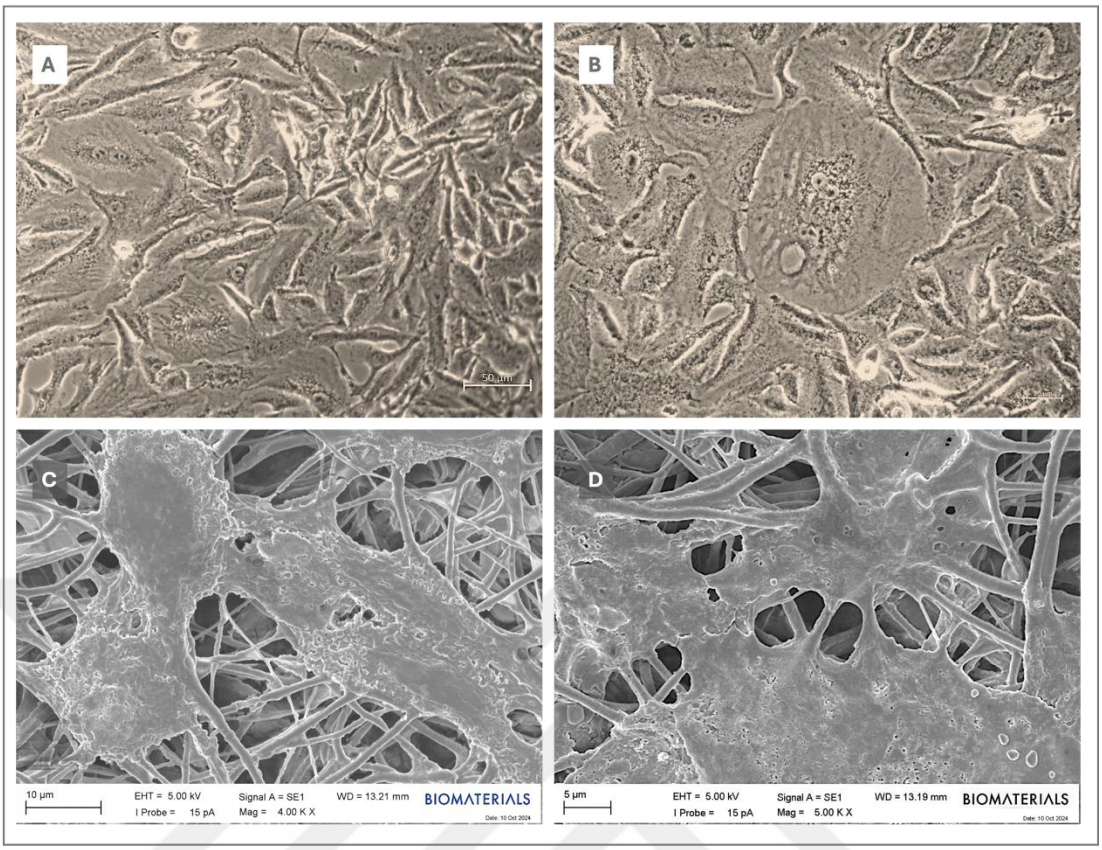

Figure 24 A549 cells grown on flat TCP surfaces and protein coated meshes. A-B) Bright field micrographs on TCP, C-D) SEM micrographs on meshes.

4.2.2 Co-culture medium optimization

MTT cell viability assay showed that the highest viability for A549 cells was observed with the 1:1 and 1:3 Endo:Epi mixtures. For pHUVEC cells, the highest viability was observed with the 3:1 Endo:Epi mixture, followed by the 1:1 mixture. Based on these results, the 1:1 mixture of epithelial and endothelial media was determined to be the optimum medium for co-culture of the cells (Figure 25).

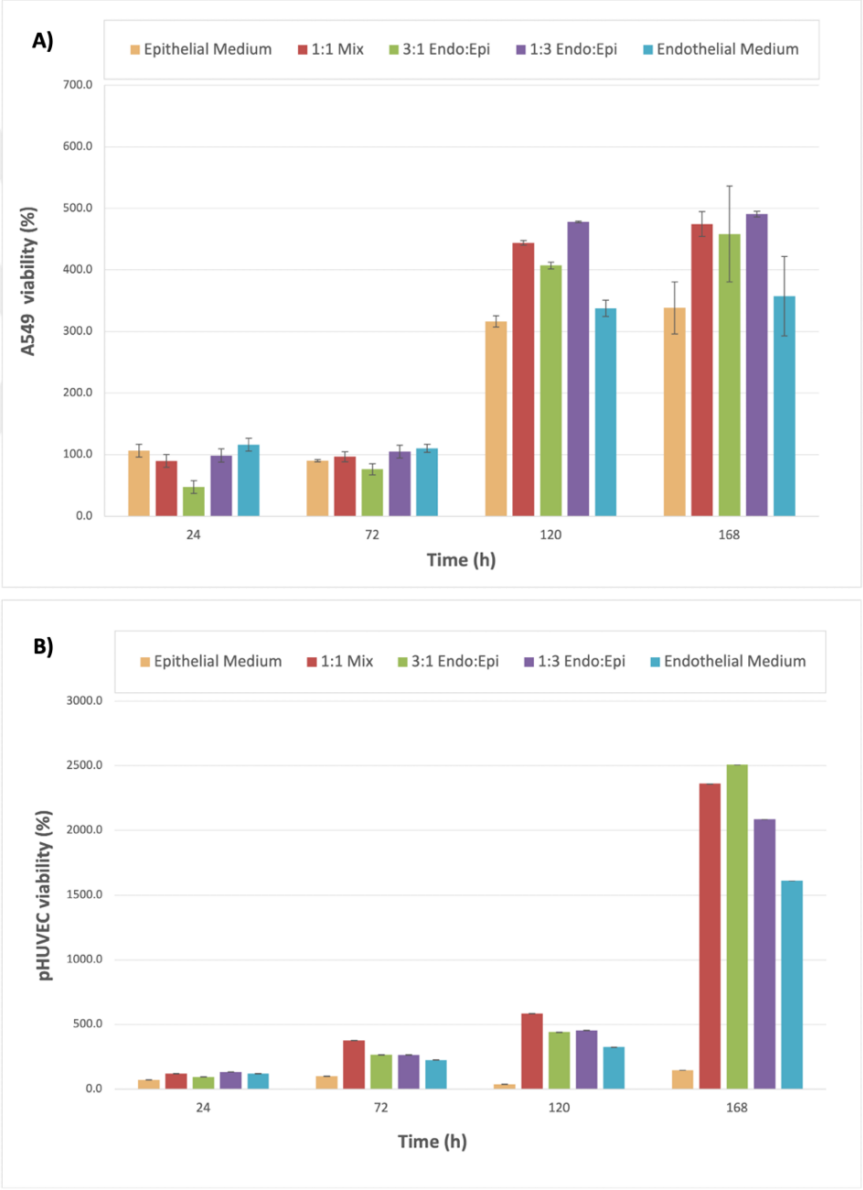

Figure 25 Co-culture medium optimization based on MTT assay: Effect of medium mixtures on A) A549, B) pHUVEC cell viability.

4.2.3 Expression of the cellular phenotypic markers on the model

The model was evaluated by determining the extent it mimics the native BAB's anatomical and spatial arrangement, as well as the expression of phenotypic markers by the cells, and surfactant secretion by the epithelial cells. The expression of the phenotypic markers by pHUVECs and A549 cells when cultured on the basement membrane mimic was studied using CLSM through IF staining of the marker proteins. For the endothelial layer, pHUVECs were shown expressing their phenotypic marker CD31, which also contributes to the formation of endothelial adherence junctions (Figure 26).

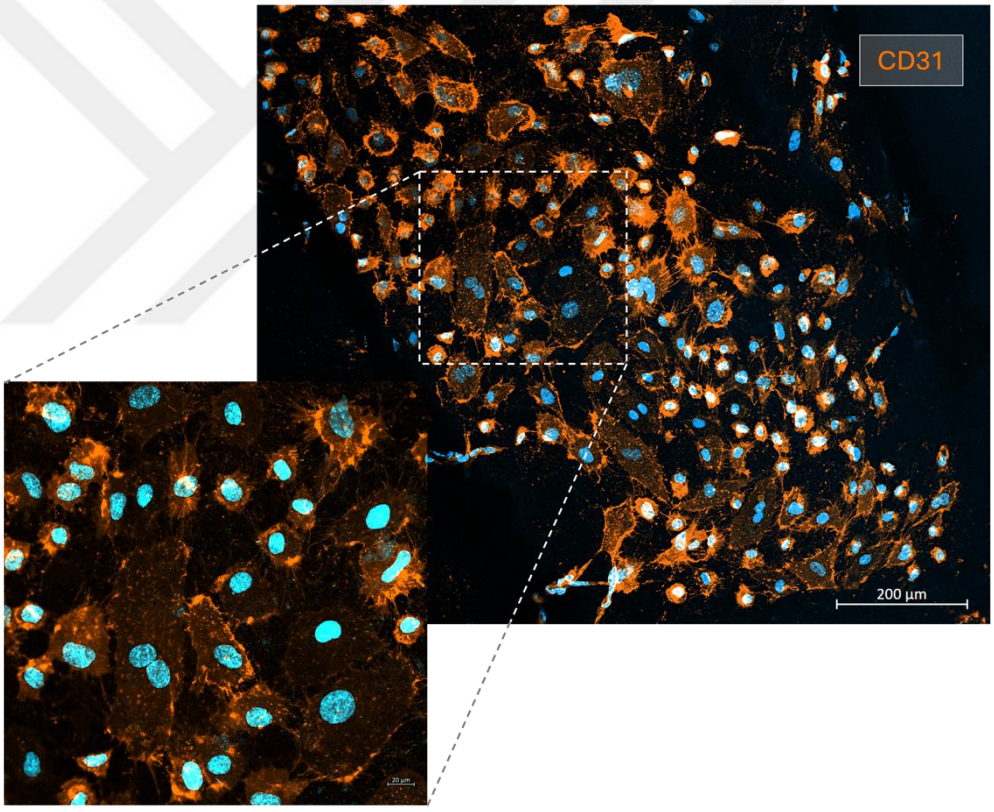

Figure 26 CLSM micrographs of pHUVECs grown on meshes for 5 days, IF stained with their phenotypic marker CD31 (orange). Nuclei stain: DAPI. Tiles scan scale bar: 200 µm, zoom in scale bar: 20 µm.

For the epithelial layer, SEM micrographs showed that both the squamous and cubical morphology present in the alveolar epithelium were presented by the cells on the mesh surface (Figure 24). This was also confirmed with CLSM micrographs, which showed the expression AETI phenotypic marker caveolin-1 and AETII phenotypic marker SP-C. Both proteins were observed in all the cells in the population but predominantly higher abundance in their corresponding phenotypes (Figure 27). This may indicate that the cells do not have a distinct but a transitional morphology. The lamellar bodies that store and secrete the surfactant components were imaged through quinacrine dihydrochloride staining. In parallel to the expression of SP-C protein, lamellar bodies were observed to be abundant in certain cells but also in the squamous AETI cells (Figure 27).

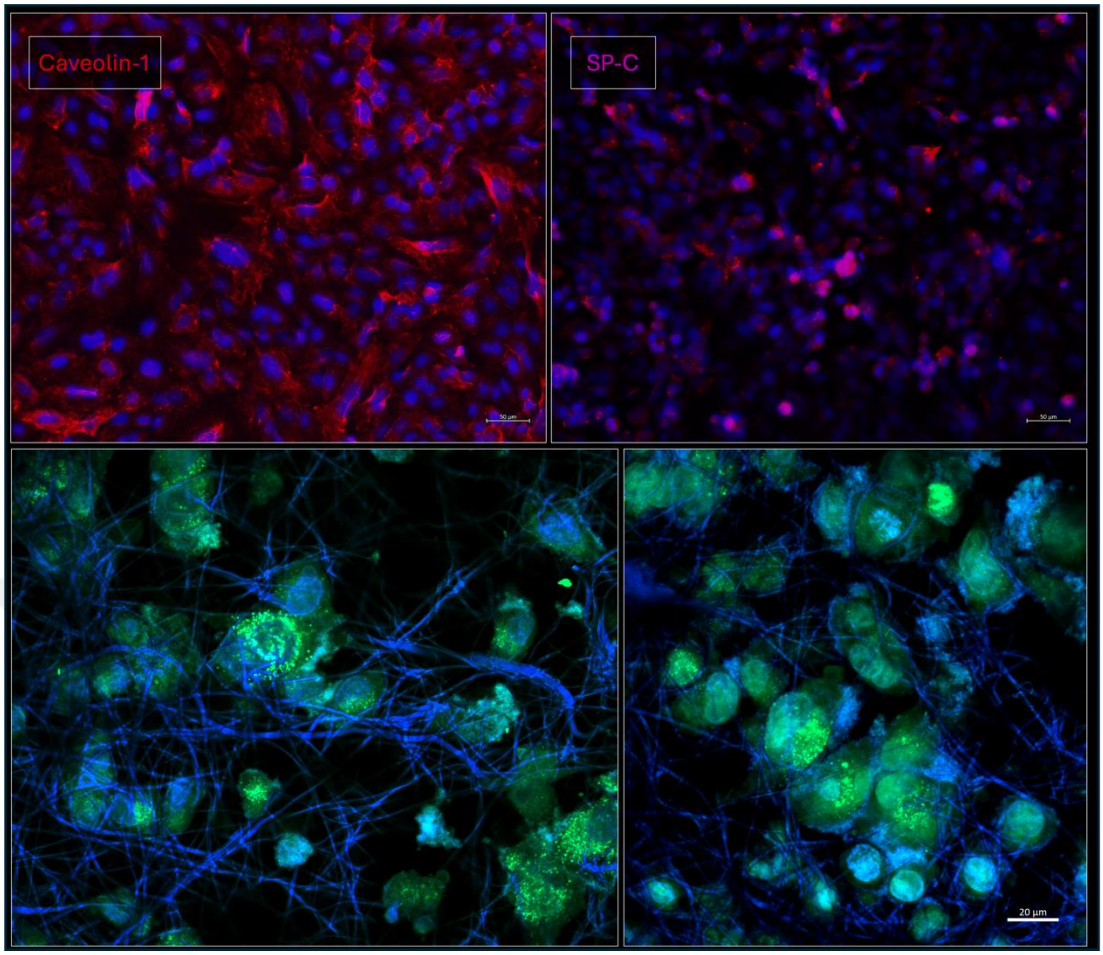

Figure 27 A549 cells grown on meshes for 4 days, A) Expressing AETI phenotypic marker Caveolin-1 (red), B) AETII phenotypic marker SP-C (magenta). Scale bar: 50 µm. C) Quinacrine dihydrochloride staining of multilamellar bodies (green). Nuclei stain: DAPI. Scale bar: 20 µm.

4.2.4 Expression of the intercellular junction proteins

The presence of intercellular junctions in the monolayers of A549 cells and pHUVECs on the scaffold was shown by IF staining of the junction proteins. pHUVEC cells grown on the mesh were shown to express CD31 and VE-Cadherin (localized mostly in the cell membranes) (Figure 29).

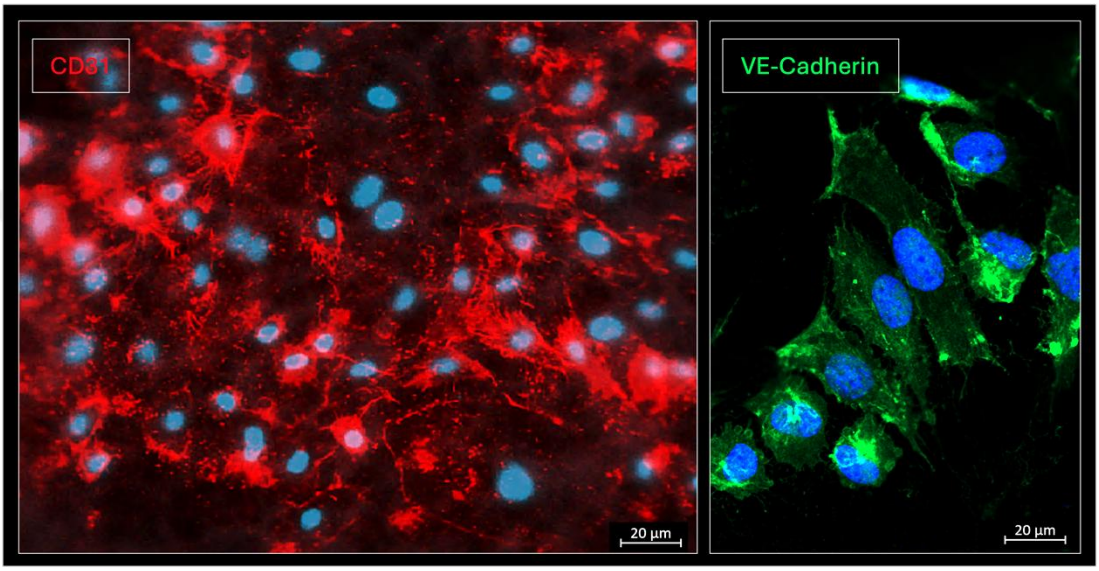

Figure 28 Fluorescence micrographs of pHUVECs IF stained with endothelial adherence junction proteins CD31 (red) and VE-Cadherin (green). Nuclei stain: DAPI (blue). Scale bar: 20 µm

Similarly, CLSM micrographs showed that A549 cells formed tight junctions by the expression of ZO-1 tight junction protein when grown on the basement membrane mimic (Figure 30).

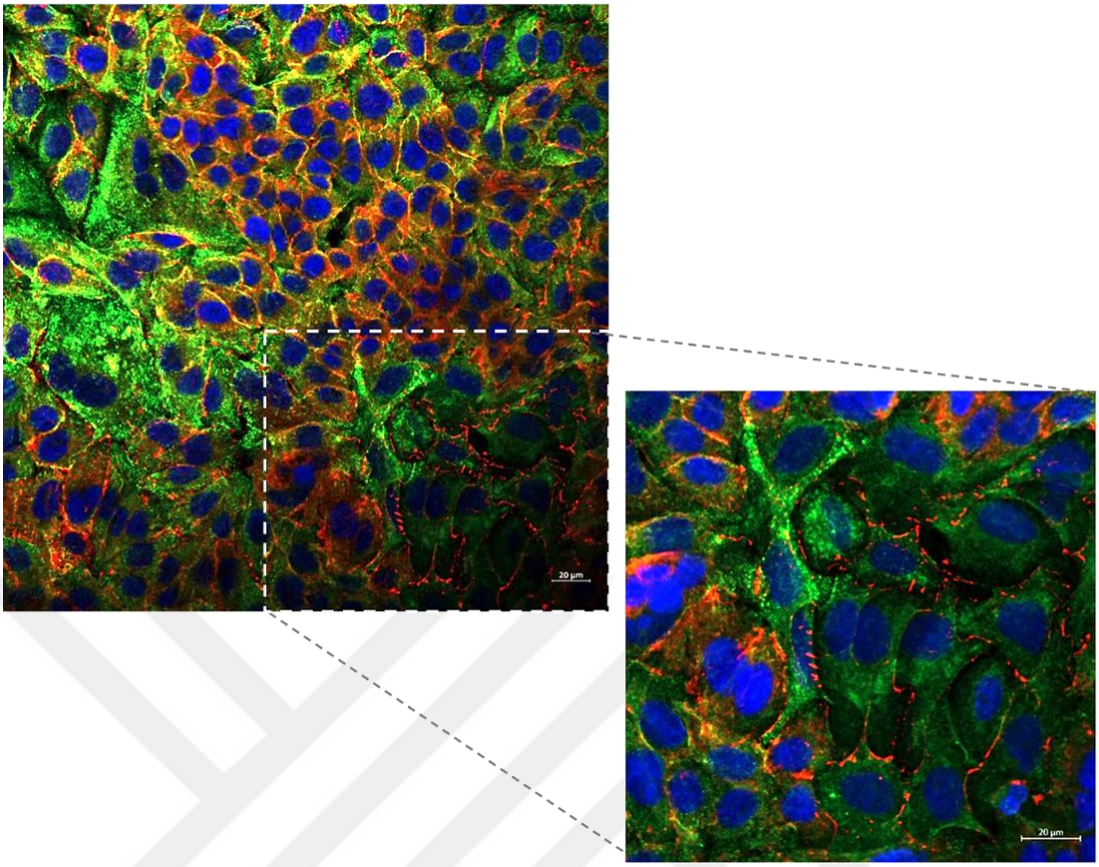

Figure 29 A549 cells grown on meshes for 10 days, IF stained with alveolar epithelial type I cell marker Caveolin-1 (green) and tight junction protein ZO-1 (red). Nuclei stain DAPI: Blue. Scale bar: 20 µm.

4.2.5 Transepithelial electrical resistance

STX4 electrodes were initially tested using a series of KCl solutions (10, 20, 40, 80, and 160 mM) in dH_2O. As the ionic concentration increased, measured resistance decreased accordingly. The values showed a logarithmic decrease within the range specified by the manufacturer, confirming the accuracy of the measurement of the electrodes (Appendix 4). TEER values of pHUVEC monoculture and epithelial-endothelial coculture showed a steady and rapid increase, respectively, reaching a plateau at ca. 44 ± 5.0 Ω.cm² from Day 7 onwards. On the other hand, A549 monoculture TEER values gradually increased, peaking at around 39.5 ± 5.5 Ω.cm² before starting to decline, ending at approximately 35 Ω.cm² by Day 14 (Figure 31). Although intercellular tight junctions formed by epithelial cells are the major contributors to the barrier integrity, lower TEER response by A549 was expected as they are a carcinoma cell line and known for forming weaker intercellular junctions (147, 148).

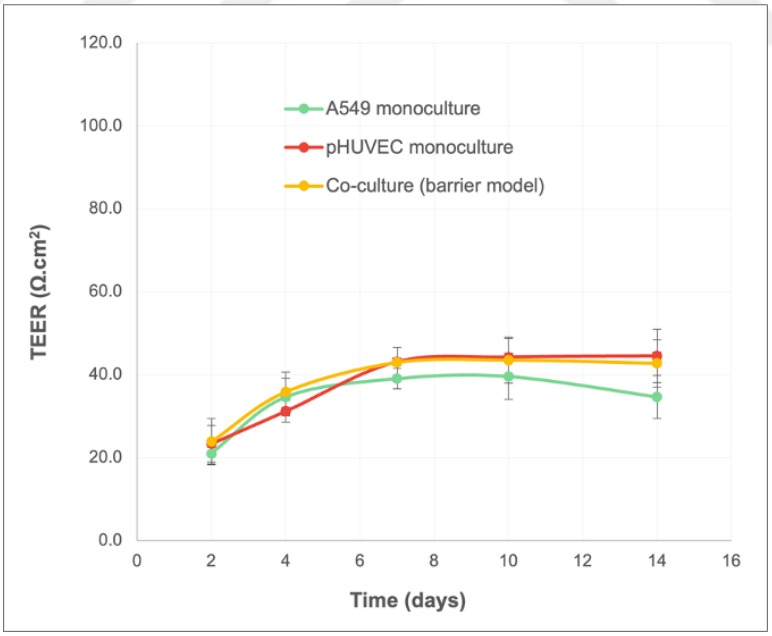

Figure 30 Change in TEER response in time for the mono- and co-culture of A549 and pHUVEC cells.

4.2.6 Permeability to sodium fluorescein and RITC-Dextran

To calculate the fraction of the molecules passed through the meshes, mass (µg) vs. relative fluorescence intensity (RFU) curves were prepared for fluorescein and RITC Dextran (Appendix 5). The fluorescein mass transport (%) calculated for the barrier model showed that the cell seeded model significantly decreased the passage of fluorescein more than the pristine or protein coated meshes, where pristine mesh showed twice the permeability (84.5%) compared to the cell seeded model (Figure 32). The average P_{app} for protein coated meshes was slightly higher than that of the barrier model, indicating that the coating provides a certain level of restriction to permeability (Table 5).

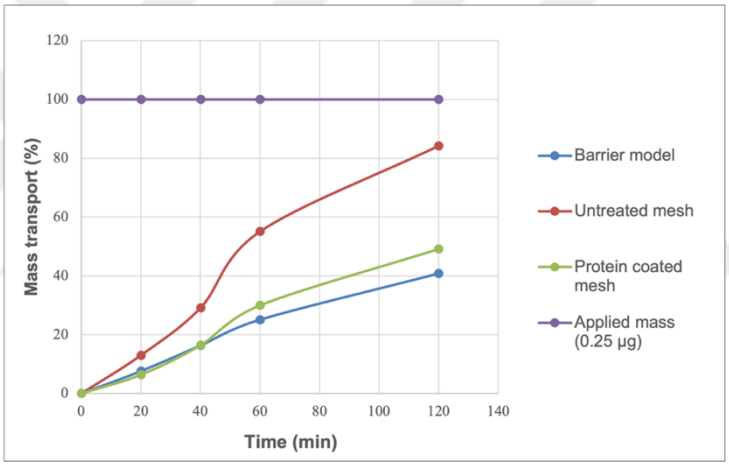

Figure 31 Fluorescein mass flux (%) through the meshes.

Table 2 Apparent permeability of the barrier model, untreated PCL mesh and protein coated mesh to Fluorescein (0.4 kDa).

	P_{app} to Fluorescein (0.4 kDa)				**Average P_{app}**	**Stdev (±)**
	20 min	**40 min**	**60 min**	**120 min**		
Barrier model	7.34×10^{-6}	1.58×10^{-5}	2.43×10^{-5}	3.95×10^{-5}	2.2×10^{-5}	1.37×10^{-5}
Untreated mesh	1.26×10^{-5}	2.82×10^{-5}	5.33×10^{-5}	8.16×10^{-5}	4.4×10^{-5}	3.02×10^{-5}
Protein coated mesh	6.17×10^{-6}	1.59×10^{-5}	2.91×10^{-5}	4.77×10^{-5}	2.5×10^{-5}	1.80×10^{-5}

4.3 SARS-CoV-2 Infection on the Model

CLSM images of the IF stained samples showed that SARS-CoV-2 virus infected the epithelium, producing its N protein and killed the cells in the barrier (Figure 33). While N protein was observed throughout the whole area of the inoculated samples, only a few cells could be detected. This was attributed to the fixation and staining protocol that likely caused the cells to wash out.

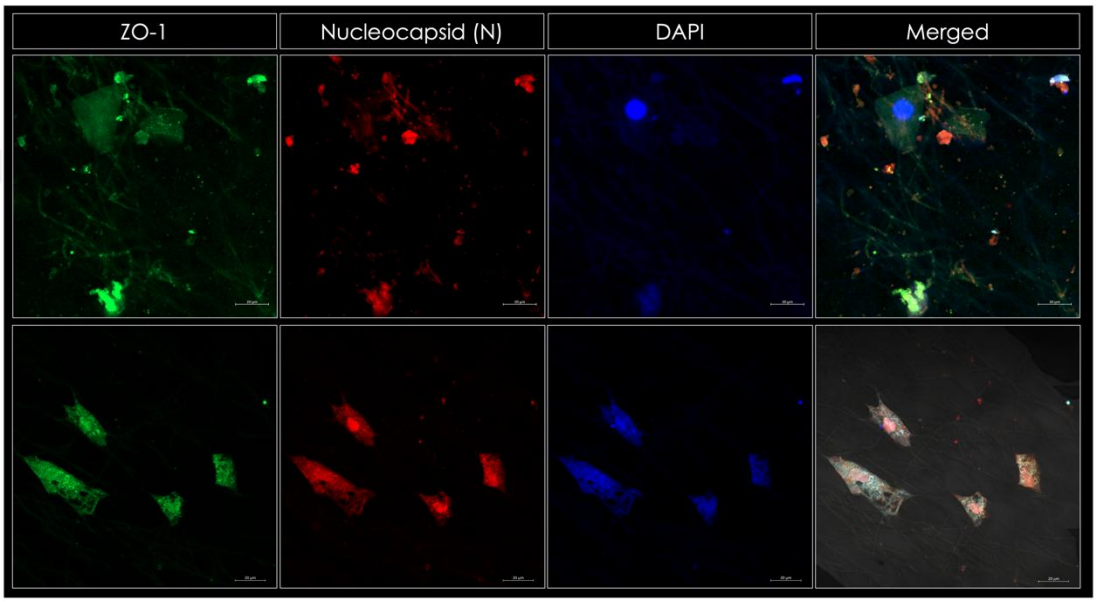

Figure 32 Alveolar epithelium in the model after SARS-CoV-2 infection (72 hpi), IF stained against ZO-1 (green), and viral nucleocapsid protein (red). Scale bar: 20 μm.

The inoculation media was kept at -80 °C for quantifying the initial viral titer (pfu/mL) that interacted with the barrier through plaque assay. The media collected at 24, 48 and 72 hpi were kept at -80 °C to assess the rate of viral propagation by the cells through RT-qPCR analysis of viral RNA. Due to time constraints, these samples were preserved for further studies.

5 DISCUSSION

This study presents a novel blood-air barrier (BAB) model for *in vitro* viral infection studies, with the aim of contributing novel insights into barrier models for studying viral infections and host response. In order to mimic the native basement membrane (BM) of the BAB, a nanofibrous PCL mesh was fabricated and coated with ECM proteins that are abundantly present in the native tissue. This basement membrane mimic was used as a scaffold to support the co-culture of epithelial and endothelial cells, forming separated monolayers on opposite sides. The diameter of the fibers (100 – 600 nm) was optimized to facilitate strong cell attachment and proliferation, and the thickness of the mesh (<20 µm) was optimized to match the thin BM of the BAB (Figure 17). Our results align with prior work that concluded electrospun nanofibers with similar dimensions support cell growth in tissue engineering applications, allowing nutrient diffusion without cell penetration (149). Compared to membranes produced from collagen or fibrin, PCL presented superior mechanical properties, durability, and ease of fabrication, making it a versatile option for long-term studies. Its structural similarity to the collagen type IV matrix, a major component of the alveolar ECM, mimics the 3D structure of the BM and creates a mechanical environment comparable to the native tissue, a feature that earlier studies using flat substrates failed to fully capture (41, 150, 151). Inclusion of the ECM proteins such as collagen type I, fibronectin and laminin 511 facilitated the formation of cellular monolayers on both epithelial and endothelial sides (Figure 20). Collagen type I is primarily known to provide mechanical stability and resilience to the tissue, while it was observed that its presence also facilitated pHUVEC attachment when used with fibronectin which is known to enhance cell adhesion by interacting with integrins on cell surface, facilitating strong cell-scaffold interactions (37, 45). Laminin, particularly laminin 511, is well known for promoting cell differentiation and stability of the alveolar epithelial monolayer (152, 153) which was shown here by the presence of lamellar bodies in AETII cells and Caveolin-1 expression in AETI cells (Figure 22, 27). The combination of these ECM molecules mimics the complex structural and signaling environment of the native alveolar-capillary interface, which is critical to consider for viral infection studies (46, 154). Respiratory viruses including SARS-

CoV-2 disrupt the ECM through the degradation of intercellular junction proteins and the remodeling of the BM, which compromises barrier integrity and leads to increased permeability (128, 148, 155). The ECM components used in this model are essential for restoring barrier integrity after viral damage and could be a focal point for therapeutic interventions aimed at reinforcing the BAB during infections. Future studies could incorporate a broader range of ECM proteins, such as elastin and nidogen, to more accurately replicate the dynamic mechanical environment of the lungs during breathing. Decellularized lung ECM can also be used, however, it is critical to determine the composition as the decellularization method affects the composition of the matrix (156). Furthermore, inclusion of HA can also be considered to mimic hyaluronan membrane formed after the infection, contributing the thickening of the barrier (46, 52).

The mesh surface became less hydrophobic (WCA of ~94°) after coating with the ECM proteins (Figure 18). While hydrophilic surfaces with a contact angle of about 60° are often preferable for cell attachment, a moderate hydrophobicity still provided an adequate environment for cell attachment and proliferation. Previous studies have indicated that moderate hydrophobicity can allow initial cell adhesion while limiting high level protein adsorption, which could hinder cell migration and growth (145, 150). The cells used in the model were well-distributed across the surface of the mesh, indicating successful seeding and adhesion to the mesh (Figure 21, 22). Both A549 and pHUVECs appeared to have attached firmly to the mesh, with their cytoplasmic extensions wrapping around the nanofibers (Figure 23, 24), a common behavior observed in cells cultured on electrospun scaffolds. The co-culture of the cells on the mesh with monolayers without contacting the cells on the other side reflected the anatomical arrangement of the native BAB.

The cobblestone morphology of pHUVECs expressing CD31 and VE-Cadherin, was visible on the endothelial side of the mesh, confirming that the cells retained their characteristics and formed a monolayer (Figure 26, 29). When cultured on flat polystyrene surfaces, HUVECs adopt a cobblestone morphology, indicative of adherence cell-cell junctions that replicate native endothelial function. This

morphology has been widely used to simulate vascular barrier integrity in previous studies, supporting the validity of the current model's use of endothelial cells in barrier research (77, 157). However, when exposed to mechanical or chemical stressors, HUVECs experience morphological changes such as cell elongation and junction disruption, reflecting endothelial permeability changes under stress conditions, as demonstrated in prior research (76, 77). Therefore, the cobblestone morphology observed here indicates an ideal HUVEC monolayer.

The A549 cells exhibited both the alveolar epithelial type I (AETI) and type II (AETII) phenotypes, as confirmed by the expression of Caveolin-1 and Surfactant Protein-C (SP-C) (Figure 27). The fluorescence micrographs showed the lamellar bodies within the A549 cells grown on the mesh, confirming that the A549 cells retained their AETII characteristics. However, it is important to note that A549 cells, while producing the surfactant, do not fully replicate the behavior of primary alveolar epithelial cells. For example, primary AETII cells can differentiate into AETI cells, whereas A549 cells predominantly retain their AETII phenotype without differentiating into AETI cells. In contrast to most studies in the field, treatment with dexamethasone to induce differentiation was avoided in order to not interfere with the host response to viral infection. Instead, this limitation was compensated by using culture media with low sugar content, and a low number of cells in seeding ($1x10^4$ cells/cm^2), and a long term culture of A549 cells in Ham's F12 Nutrient medium led to a mixed population of AETI and AETII cells in line with the previous findings (147), which was further demonstrated with the expression of tight junction protein ZO-1 in the epithelial monolayer (Figure 30).

PCL mesh had a Young's modulus of 8.07 ± 0.81 MPa (Figure 19). Although this value is higher than the typical stiffness of native basement membranes (kPa range) (33, 158), the flexibility added by collagen coating and the presence of ECM production by the cells improved the mechanical flexibility of electrospun scaffolds. However, tensile testing of the protein coated and cell seeded mesh is required to confirm if the inclusion of collagen type I enhanced the elastic properties. Studies have shown that cyclic stretch can induce cell elongation, ECM remodeling, increase in

surfactant production by the epithelium and changes in permeability, all of which are crucial for lung maturation and function (33, 36, 88). Our mesh, although mechanically stiffer than the native tissue, remained elastic within the 10% strain limit (Figure 19) that is typically observed during lung expansion and contraction (18, 151). This reflects its suitability for use in microfluidic systems where cyclic stretch is applied for studying lung mechanics and interventions like mechanical ventilation. This feature is often lacking in flat substrate-based models, which do not capture the dynamic mechanical environment of the lungs (25, 159).

Transepithelial electrical resistance (TEER) measurements indicated that the co-culture model reached a stable plateau of 44 ± 5.0 $\Omega \cdot cm^2$ by Day 7. This finding is comparable to previous work on alveolar models, where TEER values of 30-50 $\Omega \cdot cm^2$ are typical for *in vitro* models representing the alveolar-capillary interface (157, 160, 161). A slightly lower TEER observed in the A549 monoculture (39.5 ± 5.5 $\Omega \cdot cm^2$) compared to co-culture conditions is primarily due to their carcinoma origin and retention of AETII characteristics. Previous studies have similarly reported lower TEER values in carcinoma cell lines compared to primary alveolar cells, which typically form stronger intercellular junctions (157). While A549 cells are widely used for studying surfactant production and viral infections, their inability to fully transition into AETI cells limits the model's physiological relevance for studies focused on gas exchange. Higher TEER values, exceeding 200 $\Omega \cdot cm^2$, are often observed in models using primary human alveolar epithelial cells or immortalized bronchial epithelial cells like Calu-3, which form tighter junctions (12, 162). Despite these limitations, A549 cells remain a valuable tool in studying viral infections and inflammation in the alveolar epithelium. Several studies have demonstrated the susceptibility of A549 cells to SARS-CoV-2 infection when in ALI condition, and the subsequent effects on barrier integrity (148, 163). However, future iterations of this model could benefit from incorporating primary human alveolar cells or using stem cell-derived alveolar epithelial cells to more accurately represent the alveolar epithelium.

Permeability tests using fluorescein sodium and RITC-Dextran showed that the co-culture model restricted the passage of molecules, supporting its functional

integrity by limiting the diffusion of large molecules. The apparent permeability (P_{app}) values align with previous studies that employed similar permeability assays to demonstrate barrier integrity in *in vitro* lung models. In studies using in vitro lung models, the P_{app} for nicotine (0.16 kDa) was found to be 2.6×10^{-5} (164), which is consistent with our findings for fluorescein (0.4 kDa), which was 2.2×10^{-5} (Table 5). This similarity underscores the robustness of the model in mimicking native physiological conditions, particularly in its response to small molecular weight substances. Compared to standard ALI culture models with single epithelial layer at ALI, this model provides endothelial-epithelial interactions shown in previous studies that show the importance of this interaction in maintaining tight junctions.

The findings of the present study are in agreement with the existing literature, yet also provide insights into the effects of mimicking the BM by tissue engineering on cell behavior and creation of a functional barrier model to investigate barrier models in studying viral infections and host responses. The model, by simulating the native tissue environment more accurately than traditional 2D models, offers a platform for the identification of genetic factors that influence barrier function and susceptibility to viral infections. exploring potential regenerative therapies, such as stem cell-based treatments, aimed at repairing the barrier post-infection. Addition of the alveolar macrophages (AMs) into the system would permit the study of environmental and lifestyle factors, such as smoking or air pollution, which are known to exacerbate viral susceptibility and inflammation (99, 165, 166). While current literature has addressed supportive therapies in viral infections, this model expands on previous studies by incorporating host cells from various genetic backgrounds, allowing for personalized treatment approaches. This is crucial for understanding how genetic differences influence susceptibility to infections and treatment efficacy.

6 CONCLUSION

In conclusion, in this study a functional BAB model based on an electrospun PCL mesh that supports the co-culture of epithelial and endothelial cells, simulating key aspects of the BAB basement membrane was developed. While the use of A549 cells limits the model's ability to fully replicate tight barrier formation due to weak intercellular junctions indicated by the low TEER values, it is highly valuable for studying viral infections, particularly in the context of SARS-CoV-2. The scaffold's nanostructure and ECM composition consisting of collagen type I, fibronectin and laminin 511, as well as moderate elastic properties supports its suitability to be integrated into a microfluidic system, that can mimic the blood flow and cyclic stretch. The model allows using cell types with different genetic backgrounds to explore host factors influencing the infection response. It also serves as a platform for testing the efficacy of therapeutics, as well as novel drug delivery systems. Overall, this model has the potential to be widely used for respiratory research and therapeutic testing.

7 REFERENCES

1. Xu Z, Shi L, Wang Y, Zhang J, Huang L, Zhang C, et al. Pathological findings of COVID-19 associated with acute respiratory distress syndrome. Lancet Respir Med. 2020;8(4):420-2.
2. Sokolowska M, Lukasik ZM, Agache I, Akdis CA, Akdis D, Akdis M, et al. Immunology of COVID-19: Mechanisms, clinical outcome, diagnostics, and perspectives-A report of the European Academy of Allergy and Clinical Immunology (EAACI). Allergy. 2020;75(10):2445-76.
3. Knudsen L, Ochs M. The micromechanics of lung alveoli: structure and function of surfactant and tissue components. Histochem Cell Biol. 2018;150(6):661-76.
4. Mereness JA, Mariani TJ. The critical role of collagen VI in lung development and chronic lung disease. Matrix Biol Plus. 2021;10:100058.
5. Burgstaller G, Oehrle B, Gerckens M, White ES, Schiller HB, Eickelberg O. The instructive extracellular matrix of the lung: basic composition and alterations in chronic lung disease. Eur Respir J. 2017;50(1).
6. Sungnak W, Huang N, Becavin C, Berg M, Queen R, Litvinukova M, et al. SARS-CoV-2 entry factors are highly expressed in nasal epithelial cells together with innate immune genes. Nat Med. 2020;26(5):681-7.
7. Hoffmann M, Kleine-Weber H, Schroeder S, Kruger N, Herrler T, Erichsen S, et al. SARS-CoV-2 Cell Entry Depends on ACE2 and TMPRSS2 and Is Blocked by a Clinically Proven Protease Inhibitor. Cell. 2020;181(2):271-80 e8.
8. Bruce J. Colbert JJA, Karen T. Lee. Anatomy & Physiology for Health Professions: An Interactive Journey. 4 ed: Pearson Education; 2019.
9. Netter FH, Machado CAG, Hansen JT, Benninger B, Brueckner JK. Atlas of human anatomy. Philadelphia, PA: Elsevier; 2019. Available from: https://netterreference.com//content/netter_atlas_7e/?task=home.
10. West JB. A Web-based course of lectures in respiratory physiology. Adv Physiol Educ. 2011;35(3):249-51.
11. Suresh V. Permeability Properties of an In Vitro Model of the Alveolar Epithelium. Cell Mol Bioeng. 2021;14(6):653-9.
12. Rezaee F, Georas SN. Breaking barriers. New insights into airway epithelial barrier function in health and disease. Am J Respir Cell Mol Biol. 2014;50(5):857-69.
13. Weibel ER. A retrospective of lung morphometry: from 1963 to present. Am J Physiol Lung Cell Mol Physiol. 2013;305(6):L405-8.
14. Weibel ER. How to make an alveolus. Eur Respir J. 2008;31(3):483-5.
15. Townsley MI. Structure and Composition of Pulmonary Arteries, Capillaries, and Veins. Comprehensive Physiology. p. 675-709.
16. West JB, Mathieu-Costello O. Vulnerability of Pulmonary Capillaries in Heart Disease. Circulation. 1995;92(3):622-31.
17. Milhorn HT, Jr., Pulley PE, Jr. A theoretical study of pulmonary capillary gas exchange and venous admixture. Biophys J. 1968;8(3):337-57.
18. West JB, Mathieu-Costello O. Structure, strength, failure, and remodeling of the pulmonary blood-gas barrier. Annu Rev Physiol. 1999;61:543-72.
19. West J, Mathieu-Costello O. Pulmonary Blood-Gas Barrier: A Physiological Dilemma. Physiology. 1993;8(6):249-53.
20. Inoue S, Michel RP, Hogg JC. Zonulae occludentes in alveolar epithelium and capillary endothelium of dog lungs studies with the freeze-fracture technique. J Ultrastruct Res. 1976;56(2):215-25.
21. Hachenberg T, Rettig R. Stress failure of the blood-gas barrier. Curr Opin Anaesthesiol. 1998;11(1):37-44.
22. Emmler J, Hermanns MI, Steinritz D, Kreppel H, Kirkpatrick CJ, Bloch W, et al. Assessment of alterations in barrier functionality and induction of proinflammatory and cytotoxic effects after sulfur mustard exposure of an in vitro coculture model of the human alveolo-capillary barrier. Inhal Toxicol. 2007;19(8):657-65.
23. Hsia CC, Hyde DM, Weibel ER. Lung Structure and the Intrinsic Challenges of Gas Exchange. Compr Physiol. 2016;6(2):827-95.
24. Kalluri R. Basement membranes: structure, assembly and role in tumour angiogenesis. Nat Rev Cancer. 2003;3(6):422-33.

25. Jain P, Rauer SB, Möller M, Singh S. Mimicking the Natural Basement Membrane for Advanced Tissue Engineering. Biomacromolecules. 2022;23(8):3081-103.
26. Vaccaro CA, Brody JS. Structural features of alveolar wall basement membrane in the adult rat lung. J Cell Biol. 1981;91(2 Pt 1):427-37.
27. Wangensteen OD, Wittmers LE, Jr., Johnson JA. Permeability of the mammalian blood-gas barrier and its components. Am J Physiol. 1969;216(4):719-27.
28. Jayadev R, Sherwood DR. Basement membranes. Curr Biol. 2017;27(6):R207-R11.
29. Dunsmore SE, Rannels DE. Extracellular matrix biology in the lung. Am J Physiol. 1996;270(1 Pt 1):L3-27.
30. Tsuchiya T, Doi R, Obata T, Hatachi G, Nagayasu T. Lung Microvascular Niche, Repair, and Engineering. Front Bioeng Biotechnol. 2020;8:105.
31. Pozzi A, Yurchenco PD, Iozzo RV. The nature and biology of basement membranes. Matrix Biol. 2017;57-58:1-11.
32. Drain AP, Weaver VM. Chapter 7 - Matrix molecules and their ligands. In: Lanza R, Langer R, Vacanti JP, Atala A, editors. Principles of Tissue Engineering (Fifth Edition): Academic Press; 2020. p. 119-32.
33. Maina JN, West JB. Thin and strong! The bioengineering dilemma in the structural and functional design of the blood-gas barrier. Physiol Rev. 2005;85(3):811-44.
34. Basak T, Vega-Montoto L, Zimmerman LJ, Tabb DL, Hudson BG, Vanacore RM. Comprehensive Characterization of Glycosylation and Hydroxylation of Basement Membrane Collagen IV by High-Resolution Mass Spectrometry. J Proteome Res. 2016;15(1):245-58.
35. Timpl R, Wiedemann H, van Delden V, Furthmayr H, Kuhn K. A network model for the organization of type IV collagen molecules in basement membranes. Eur J Biochem. 1981;120(2):203-11.
36. Hsieh A, Yang CX, Al-Fouadi M, Nwozor KO, Osei ET, Hackett TL. The contribution of reticular basement membrane proteins to basal airway epithelial attachment, spreading and barrier formation: implications for airway remodeling in asthma. Front Med (Lausanne). 2023;10:1214130.
37. Kleinman HK, Wilkes CM, Martin GR. Interaction of fibronectin with collagen fibrils. Biochemistry. 1981;20(8):2325-30.
38. Siu MK, Lee WM, Cheng CY. The interplay of collagen IV, tumor necrosis factor-alpha, gelatinase B (matrix metalloprotease-9), and tissue inhibitor of metalloproteases-1 in the basal lamina regulates Sertoli cell-tight junction dynamics in the rat testis. Endocrinology. 2003;144(1):371-87.
39. Dudek SM, Garcia JG. Cytoskeletal regulation of pulmonary vascular permeability. J Appl Physiol (1985). 2001;91(4):1487-500.
40. Cescon M, Gattazzo F, Chen P, Bonaldo P. Collagen VI at a glance. J Cell Sci. 2015;128(19):3525-31.
41. Cavalcante FS, Ito S, Brewer K, Sakai H, Alencar AM, Almeida MP, et al. Mechanical interactions between collagen and proteoglycans: implications for the stability of lung tissue. J Appl Physiol (1985). 2005;98(2):672-9.
42. Mecham RP. Elastin in lung development and disease pathogenesis. Matrix Biol. 2018;73:6-20.
43. Menezes MJ, McClenahan FK, Leiton CV, Aranmolate A, Shan X, Colognato H. The Extracellular Matrix Protein Laminin α2 Regulates the Maturation and Function of the Blood–Brain Barrier. The Journal of Neuroscience. 2014;34(46):15260-80.
44. Morrissey MA, Sherwood DR. An active role for basement membrane assembly and modification in tissue sculpting. J Cell Sci. 2015;128(9):1661-8.
45. Kubow KE, Vukmirovic R, Zhe L, Klotzsch E, Smith ML, Gourdon D, et al. Mechanical forces regulate the interactions of fibronectin and collagen I in extracellular matrix. Nat Commun. 2015;6:8026.
46. Singh B, Fleury C, Jalalvand F, Riesbeck K. Human pathogens utilize host extracellular matrix proteins laminin and collagen for adhesion and invasion of the host. FEMS Microbiol Rev. 2012;36(6):1122-80.
47. Blanchette M, Daneman R. Formation and maintenance of the BBB. Mech Dev. 2015;138 Pt 1:8-16.
48. Goldenberg NM, Kuebler WM. Endothelial cell regulation of pulmonary vascular tone, inflammation, and coagulation. Compr Physiol. 2015;5(2):531-59.
49. Chang YT, Tseng CN, Tannenberg P, Eriksson L, Yuan K, de Jesus Perez VA, et al. Perlecan heparan sulfate deficiency impairs pulmonary vascular development and attenuates hypoxic pulmonary hypertension. Cardiovasc Res. 2015;107(1):20-31.
50. Whitelock JM, Melrose J, Iozzo RV. Diverse cell signaling events modulated by perlecan. Biochemistry. 2008;47(43):11174-83.

51. Karjalainen EM, Lindqvist A, Laitinen LA, Kava T, Altraja A, Halme M, et al. Airway inflammation and basement membrane tenascin in newly diagnosed atopic and nonatopic asthma. Respir Med. 2003;97(9):1045-51.
52. Bell TJ, Brand OJ, Morgan DJ, Salek-Ardakani S, Jagger C, Fujimori T, et al. Defective lung function following influenza virus is due to prolonged, reversible hyaluronan synthesis. Matrix Biol. 2019;80:14-28.
53. Schiller HB, Fernandez IE, Burgstaller G, Schaab C, Scheltema RA, Schwarzmayr T, et al. Time- and compartment-resolved proteome profiling of the extracellular niche in lung injury and repair. Mol Syst Biol. 2015;11(7):819.
54. Annoni R, Lancas T, Yukimatsu Tanigawa R, de Medeiros Matsushita M, de Morais Fernezlian S, Bruno A, et al. Extracellular matrix composition in COPD. Eur Respir J. 2012;40(6):1362-73.
55. Matthes SA, Hadley R, Roman J, White ES. Chapter 20 - Comparative Biology of the Normal Lung Extracellular Matrix. In: Parent RA, editor. Comparative Biology of the Normal Lung (Second Edition). San Diego: Academic Press; 2015. p. 387-402.
56. Weibel ER. On the tricks alveolar epithelial cells play to make a good lung. Am J Respir Crit Care Med. 2015;191(5):504-13.
57. Ruaro B, Salton F, Braga L, Wade B, Confalonieri P, Volpe MC, et al. The History and Mystery of Alveolar Epithelial Type II Cells: Focus on Their Physiologic and Pathologic Role in Lung. Int J Mol Sci. 2021;22(5).
58. Overgaard CE, Mitchell LA, Koval M. Roles for claudins in alveolar epithelial barrier function. Ann N Y Acad Sci. 2012;1257(1):167-74.
59. Diem K, Fauler M, Fois G, Hellmann A, Winokurow N, Schumacher S, et al. Mechanical stretch activates piezo1 in caveolae of alveolar type I cells to trigger ATP release and paracrine stimulation of surfactant secretion from alveolar type II cells. FASEB J. 2020;34(9):12785-804.
60. Haller T, Ortmayr J, Friedrich F, Volkl H, Dietl P. Dynamics of surfactant release in alveolar type II cells. Proc Natl Acad Sci U S A. 1998;95(4):1579-84.
61. Ochs M, Hegermann J, Lopez-Rodriguez E, Timm S, Nouailles G, Matuszak J, et al. On Top of the Alveolar Epithelium: Surfactant and the Glycocalyx. Int J Mol Sci. 2020;21(9).
62. Weaver TE, Na CL, Stahlman M. Biogenesis of lamellar bodies, lysosome-related organelles involved in storage and secretion of pulmonary surfactant. Semin Cell Dev Biol. 2002;13(4):263-70.
63. Garcia-Mouton C, Hidalgo A, Cruz A, Perez-Gil J. The Lord of the Lungs: The essential role of pulmonary surfactant upon inhalation of nanoparticles. Eur J Pharm Biopharm. 2019;144:230-43.
64. Pioselli B, Salomone F, Mazzola G, Amidani D, Sgarbi E, Amadei F, et al. Pulmonary Surfactant: A Unique Biomaterial with Life-saving Therapeutic Applications. Curr Med Chem. 2022;29(3):526-90.
65. Perez-Gil J. A recipe for a good clinical pulmonary surfactant. Biomed J. 2022;45(4):615-28.
66. Korolainen H, Lolicato F, Enkavi G, Perez-Gil J, Kulig W, Vattulainen I. Dimerization of the pulmonary surfactant protein C in a membrane environment. PLoS One. 2022;17(4):e0267155.
67. Moran-Lalangui M, Coutinho A, Prieto M, Fedorov A, Perez-Gil J, Loura LMS, et al. Exploring protein-protein interactions and oligomerization state of pulmonary surfactant protein C (SP-C) through FRET and fluorescence self-quenching. Protein Sci. 2024;33(1):e4835.
68. Estrada P, Banares-Hidalgo A, Perez-Gil J. Disulfide bonds in the SAPA domain of the pulmonary surfactant protein B precursor. J Proteomics. 2022;269:104722.
69. Parra E, Perez-Gil J. Composition, structure and mechanical properties define performance of pulmonary surfactant membranes and films. Chem Phys Lipids. 2015;185:153-75.
70. Castillo-Sanchez JC, Cruz A, Perez-Gil J. Structural hallmarks of lung surfactant: Lipid-protein interactions, membrane structure and future challenges. Arch Biochem Biophys. 2021;703:108850.
71. Radiom M, Sarkis M, Brookes O, Oikonomou EK, Baeza-Squiban A, Berret JF. Pulmonary surfactant inhibition of nanoparticle uptake by alveolar epithelial cells. Sci Rep. 2020;10(1):19436.
72. Han S, Mallampalli RK. The Role of Surfactant in Lung Disease and Host Defense against Pulmonary Infections. Ann Am Thorac Soc. 2015;12(5):765-74.
73. Nguyen HA, Rajaram MV, Meyer DA, Schlesinger LS. Pulmonary surfactant protein A and surfactant lipids upregulate IRAK-M, a negative regulator of TLR-mediated inflammation in human macrophages. Am J Physiol Lung Cell Mol Physiol. 2012;303(7):L608-16.
74. Watson A, Madsen J, Clark HW. SP-A and SP-D: Dual Functioning Immune Molecules With Antiviral and Immunomodulatory Properties. Front Immunol. 2020;11:622598.
75. Simmons S, Erfinanda L, Bartz C, Kuebler WM. Novel mechanisms regulating endothelial barrier function in the pulmonary microcirculation. J Physiol. 2019;597(4):997-1021.

76. Fang Y, Wu D, Birukov KG. Mechanosensing and Mechanoregulation of Endothelial Cell Functions. Compr Physiol. 2019;9(2):873-904.
77. Steward R, Jr., Tambe D, Hardin CC, Krishnan R, Fredberg JJ. Fluid shear, intercellular stress, and endothelial cell alignment. Am J Physiol Cell Physiol. 2015;308(8):C657-64.
78. Giannotta M, Trani M, Dejana E. VE-cadherin and endothelial adherens junctions: active guardians of vascular integrity. Dev Cell. 2013;26(5):441-54.
79. Reitsma S, Slaaf DW, Vink H, van Zandvoort MA, oude Egbrink MG. The endothelial glycocalyx: composition, functions, and visualization. Pflugers Arch. 2007;454(3):345-59.
80. Parthasarathi K. The Pulmonary Vascular Barrier: Insights into Structure, Function, and Regulatory Mechanisms. Adv Anat Embryol Cell Biol. 2018;228:41-61.
81. Dragovich MA, Chester D, Fu BM, Wu C, Xu Y, Goligorsky MS, et al. Mechanotransduction of the endothelial glycocalyx mediates nitric oxide production through activation of TRP channels. American Journal of Physiology-Cell Physiology. 2016;311(6):C846-C53.
82. Raychaudhuri B, Fisher CJ, Farver CF, Malur A, Drazba J, Kavuru MS, et al. Interleukin 10 (IL-10)-mediated inhibition of inflammatory cytokine production by human alveolar macrophages. Cytokine. 2000;12(9):1348-55.
83. Guilliams M, Lambrecht BN, Hammad H. Division of labor between lung dendritic cells and macrophages in the defense against pulmonary infections. Mucosal Immunol. 2013;6(3):464-73.
84. Channappanavar R, Fehr AR, Vijay R, Mack M, Zhao J, Meyerholz DK, et al. Dysregulated Type I Interferon and Inflammatory Monocyte-Macrophage Responses Cause Lethal Pneumonia in SARS-CoV-Infected Mice. Cell Host Microbe. 2016;19(2):181-93.
85. Hussell T, Bell TJ. Alveolar macrophages: plasticity in a tissue-specific context. Nat Rev Immunol. 2014;14(2):81-93.
86. Han S, Mallampalli RK. The acute respiratory distress syndrome: from mechanism to translation. J Immunol. 2015;194(3):855-60.
87. Booth AJ, Hadley R, Cornett AM, Dreffs AA, Matthes SA, Tsui JL, et al. Acellular normal and fibrotic human lung matrices as a culture system for in vitro investigation. Am J Respir Crit Care Med. 2012;186(9):866-76.
88. Chung AS, Kao WJ. Fibroblasts regulate monocyte response to ECM-derived matrix: the effects on monocyte adhesion and the production of inflammatory, matrix remodeling, and growth factor proteins. J Biomed Mater Res A. 2009;89(4):841-53.
89. West JB. Comparative physiology of the pulmonary circulation. Compr Physiol. 2011;1(3):1525-39.
90. West JB, Wang DL, Prisk GK, Fine JM, Bellinghausen A, Light M, et al. Noninvasive measurement of pulmonary gas exchange: comparison with data from arterial blood gases. Am J Physiol Lung Cell Mol Physiol. 2019;316(1):L114-L8.
91. West JB. Internet-based course on pulmonary pathophysiology. Adv Physiol Educ. 2012;36(1):1-2.
92. West JB. A lifetime of pulmonary gas exchange. Physiol Rep. 2018;6(20):e13903.
93. Weibel ER. Lung morphometry: the link between structure and function. Cell Tissue Res. 2017;367(3):413-26.
94. Widrich J, Shetty M. Physiology, Pulmonary Vascular Resistance. StatPearls. Treasure Island (FL)2024.
95. Martin TR, Frevert CW. Innate immunity in the lungs. Proc Am Thorac Soc. 2005;2(5):403-11.
96. Thomas RJ. Particle size and pathogenicity in the respiratory tract. Virulence. 2013;4(8):847-58.
97. Heyder JPD, Gebhart J, Rudolf G, Schiller C, Stahlhofen W. Deposition of particles in the human respiratory tract in the size range 0.005–15 μm. Journal of Aerosol Science. 1986;17:811-25.
98. Brain JD. Lung macrophages: how many kinds are there? What do they do? Am Rev Respir Dis. 1988;137(3):507-9.
99. Allard B, Panariti A, Martin JG. Alveolar Macrophages in the Resolution of Inflammation, Tissue Repair, and Tolerance to Infection. Front Immunol. 2018;9:1777.
100. Schneider C, Nobs SP, Heer AK, Kurrer M, Klinke G, van Rooijen N, et al. Alveolar macrophages are essential for protection from respiratory failure and associated morbidity following influenza virus infection. PLoS Pathog. 2014;10(4):e1004053.
101. Gil M, McCormack FX, Levine AM. Surfactant protein A modulates cell surface expression of CR3 on alveolar macrophages and enhances CR3-mediated phagocytosis. J Biol Chem. 2009;284(12):7495-504.
102. Li MO, Wan YY, Sanjabi S, Robertson AK, Flavell RA. Transforming growth factor-beta regulation of immune responses. Annu Rev Immunol. 2006;24:99-146.

103. Werner F, Jain MK, Feinberg MW, Sibinga NE, Pellacani A, Wiesel P, et al. Transforming growth factor-beta 1 inhibition of macrophage activation is mediated via Smad3. J Biol Chem. 2000;275(47):36653-8.
104. Hanchard J, Capo-Velez CM, Deusch K, Lidington D, Bolz SS. Stabilizing Cellular Barriers: Raising the Shields Against COVID-19. Front Endocrinol (Lausanne). 2020;11:583006.
105. Subbarao K, Mahanty S. Respiratory Virus Infections: Understanding COVID-19. Immunity. 2020;52(6):905-9.
106. Cilloniz C, Luna CM, Hurtado JC, Marcos MA, Torres A. Respiratory viruses: their importance and lessons learned from COVID-19. Eur Respir Rev. 2022;31(166).
107. Zhou P, Yang XL, Wang XG, Hu B, Zhang L, Zhang W, et al. A pneumonia outbreak associated with a new coronavirus of probable bat origin. Nature. 2020;579(7798):270-3.
108. Mason RJ. Pathogenesis of COVID-19 from a cell biology perspective. Eur Respir J. 2020;55(4).
109. Hou YJ, Okuda K, Edwards CE, Martinez DR, Asakura T, Dinnon KH, 3rd, et al. SARS-CoV-2 Reverse Genetics Reveals a Variable Infection Gradient in the Respiratory Tract. Cell. 2020;182(2):429-46 e14.
110. Shang J, Ye G, Shi K, Wan Y, Luo C, Aihara H, et al. Structural basis of receptor recognition by SARS-CoV-2. Nature. 2020;581(7807):221-4.
111. Sims AC, Baric RS, Yount B, Burkett SE, Collins PL, Pickles RJ. Severe acute respiratory syndrome coronavirus infection of human ciliated airway epithelia: role of ciliated cells in viral spread in the conducting airways of the lungs. J Virol. 2005;79(24):15511-24.
112. Wolfel R, Corman VM, Guggemos W, Seilmaier M, Zange S, Muller MA, et al. Virological assessment of hospitalized patients with COVID-2019. Nature. 2020;581(7809):465-9.
113. Dinarello CA. Proinflammatory cytokines. Chest. 2000;118(2):503-8.
114. Johansson C, Kirsebom FCM. Neutrophils in respiratory viral infections. Mucosal Immunol. 2021;14(4):815-27.
115. Wiersinga WJ, Rhodes A, Cheng AC, Peacock SJ, Prescott HC. Pathophysiology, Transmission, Diagnosis, and Treatment of Coronavirus Disease 2019 (COVID-19): A Review. JAMA. 2020;324(8):782-93.
116. Gentile F, Aimo A, Forfori F, Catapano G, Clemente A, Cademartiri F, et al. COVID-19 and risk of pulmonary fibrosis: the importance of planning ahead. Eur J Prev Cardiol. 2020;27(13):1442-6.
117. Deinhardt-Emmer S, Bottcher S, Haring C, Giebeler L, Henke A, Zell R, et al. SARS-CoV-2 causes severe epithelial inflammation and barrier dysfunction. J Virol. 2021;95(10).
118. Xu G, Qi F, Li H, Yang Q, Wang H, Wang X, et al. The differential immune responses to COVID-19 in peripheral and lung revealed by single-cell RNA sequencing. Cell Discov. 2020;6:73.
119. Mehta P, McAuley DF, Brown M, Sanchez E, Tattersall RS, Manson JJ, et al. COVID-19: consider cytokine storm syndromes and immunosuppression. Lancet. 2020;395(10229):1033-4.
120. Velavan TP, Pallerla SR, Ruter J, Augustin Y, Kremsner PG, Krishna S, et al. Host genetic factors determining COVID-19 susceptibility and severity. EBioMedicine. 2021;72:103629.
121. Guo H, Hu BJ, Yang XL, Zeng LP, Li B, Ouyang S, et al. Evolutionary Arms Race between Virus and Host Drives Genetic Diversity in Bat Severe Acute Respiratory Syndrome-Related Coronavirus Spike Genes. J Virol. 2020;94(20).
122. Wang Q, Doerschuk CM. Neutrophil-induced changes in the biomechanical properties of endothelial cells: roles of ICAM-1 and reactive oxygen species. J Immunol. 2000;164(12):6487-94.
123. Brouki Milan P, Masoumi F, Biazar E, Zare Jalise S, Mehrabi A. Exploiting the Potential of Decellularized Extracellular Matrix (ECM) in Tissue Engineering: A Review Study. Macromol Biosci. 2024:e2400322.
124. McMahon M, Ye S, Pedrina J, Dlugolenski D, Stambas J. Extracellular Matrix Enzymes and Immune Cell Biology. Front Mol Biosci. 2021;8:703868.
125. Bhowmick R, Derakhshan T, Liang Y, Ritchey J, Liu L, Gappa-Fahlenkamp H. A Three-Dimensional Human Tissue-Engineered Lung Model to Study Influenza A Infection. Tissue Eng Part A. 2018;24(19-20):1468-80.
126. Huang D, Liu T, Liao J, Maharjan S, Xie X, Perez M, et al. Reversed-engineered human alveolar lung-on-a-chip model. Proc Natl Acad Sci U S A. 2021;118(19).
127. Tan J, Guo Q, Tian L, Pei Z, Li D, Wu M, et al. Biomimetic lung-on-a-chip to model virus infection and drug evaluation. Eur J Pharm Sci. 2023;180:106329.
128. Youk J, Kim T, Evans KV, Jeong YI, Hur Y, Hong SP, et al. Three-Dimensional Human Alveolar Stem Cell Culture Models Reveal Infection Response to SARS-CoV-2. Cell Stem Cell. 2020;27(6):905-19 e10.

129. Zhang M, Wang P, Luo R, Wang Y, Li Z, Guo Y, et al. Biomimetic Human Disease Model of SARS-CoV-2-Induced Lung Injury and Immune Responses on Organ Chip System. Adv Sci (Weinh). 2021;8(3):2002928.
130. Zhang M, Xu C, Jiang L, Qin J. A 3D human lung-on-a-chip model for nanotoxicity testing. Toxicol Res (Camb). 2018;7(6):1048-60.
131. Mulay A, Konda B, Garcia G, Jr., Yao C, Beil S, Villalba JM, et al. SARS-CoV-2 infection of primary human lung epithelium for COVID-19 modeling and drug discovery. Cell Rep. 2021;35(5):109055.
132. Yang X, Li K, Zhang X, Liu C, Guo B, Wen W, et al. Nanofiber membrane supported lung-on-a-chip microdevice for anti-cancer drug testing. Lab Chip. 2018;18(3):486-95.
133. Dohle E, Singh S, Nishigushi A, Fischer T, Wessling M, Moller M, et al. Human Co- and Triple-Culture Model of the Alveolar-Capillary Barrier on a Basement Membrane Mimic. Tissue Eng Part C Methods. 2018;24(9):495-503.
134. Dekali S, Gamez C, Rogerieux F, Rat P, Lacroix G. Characterization of a new coculture model of alveolo-capillary barrier developed to study the translocation and the toxicity of nanoparticles. Toxicology Letters. 2011;205:S156.
135. Johnson DC, McFadden G. Viral Immune Evasion. Immunology of Infectious Diseases2001. p. 357-77.
136. Lee HC, Chathuranga K, Lee JS. Intracellular sensing of viral genomes and viral evasion. Exp Mol Med. 2019;51(12):1-13.
137. McFadden MJ, Horner SM. N(6)-Methyladenosine Regulates Host Responses to Viral Infection. Trends Biochem Sci. 2021;46(5):366-77.
138. Birgersdotter A, Sandberg R, Ernberg I. Gene expression perturbation in vitro--a growing case for three-dimensional (3D) culture systems. Semin Cancer Biol. 2005;15(5):405-12.
139. Bauer CM, Dewitte-Orr SJ, Hornby KR, Zavitz CC, Lichty BD, Stampfli MR, et al. Cigarette smoke suppresses type I interferon-mediated antiviral immunity in lung fibroblast and epithelial cells. J Interferon Cytokine Res. 2008;28(3):167-79.
140. Proud D, Hudy MH, Wiehler S, Zaheer RS, Amin MA, Pelikan JB, et al. Cigarette smoke modulates expression of human rhinovirus-induced airway epithelial host defense genes. PLoS One. 2012;7(7):e40762.
141. Eddleston J, Lee RU, Doerner AM, Herschbach J, Zuraw BL. Cigarette smoke decreases innate responses of epithelial cells to rhinovirus infection. Am J Respir Cell Mol Biol. 2011;44(1):118-26.
142. Duffney PF, McCarthy CE, Nogales A, Thatcher TH, Martinez-Sobrido L, Phipps RP, et al. Cigarette smoke dampens antiviral signaling in small airway epithelial cells by disrupting TLR3 cleavage. Am J Physiol Lung Cell Mol Physiol. 2018;314(3):L505-L13.
143. Schneider CA, Rasband WS, Eliceiri KW. NIH Image to ImageJ: 25 years of image analysis. Nat Methods. 2012;9(7):671-5.
144. Hanifehnezhad A, Kehribar ES, Oztop S, Sheraz A, Kasirga S, Ergunay K, et al. Characterization of local SARS-CoV-2 isolates and pathogenicity in IFNAR(-/-) mice. Heliyon. 2020;6(9):e05116.
145. Nossa R, Costa J, Cacopardo L, Ahluwalia A. Breathing in vitro: Designs and applications of engineered lung models. J Tissue Eng. 2021;12:20417314211008696.
146. Harris AF, Lacombe J, Sanchez-Ballester NM, Victor S, Curran KAJ, Nordquist AR, et al. Decellularized Spinach Biomaterials Support Physiologically Relevant Mechanical Cyclic Strain and Prompt a Stretch-Induced Cellular Response. ACS Appl Bio Mater. 2022;5(12):5682-92.
147. Cooper JR, Abdullatif MB, Burnett EC, Kempsell KE, Conforti F, Tolley H, et al. Long Term Culture of the A549 Cancer Cell Line Promotes Multilamellar Body Formation and Differentiation towards an Alveolar Type II Pneumocyte Phenotype. PLoS One. 2016;11(10):e0164438.
148. Sasaki M, Kishimoto M, Itakura Y, Tabata K, Intaruck K, Uemura K, et al. Air-liquid interphase culture confers SARS-CoV-2 susceptibility to A549 alveolar epithelial cells. Biochem Biophys Res Commun. 2021;577:146-51.
149. Wang X, Ding B, Li B. Biomimetic electrospun nanofibrous structures for tissue engineering. Mater Today (Kidlington). 2013;16(6):229-41.
150. Doryab A, Tas S, Taskin MB, Yang L, Hilgendorff A, Groll J, et al. Evolution of Bioengineered Lung Models: Recent Advances and Challenges in Tissue Mimicry for Studying the Role of Mechanical Forces in Cell Biology. Advanced Functional Materials. 2019;29(39):1903114.
151. Guenat OT, Berthiaume F. Incorporating mechanical strain in organs-on-a-chip: Lung and skin. Biomicrofluidics. 2018;12(4):042207.

152. Nguyen NM, Kelley DG, Schlueter JA, Meyer MJ, Senior RM, Miner JH. Epithelial laminin alpha5 is necessary for distal epithelial cell maturation, VEGF production, and alveolization in the developing murine lung. Dev Biol. 2005;282(1):111-25.
153. Song J, Zhang X, Buscher K, Wang Y, Wang H, Di Russo J, et al. Endothelial Basement Membrane Laminin 511 Contributes to Endothelial Junctional Tightness and Thereby Inhibits Leukocyte Transmigration. Cell Rep. 2017;18(5):1256-69.
154. Higuita-Castro N, Nelson MT, Shukla V, Agudelo-Garcia PA, Zhang W, Duarte-Sanmiguel SM, et al. Using a Novel Microfabricated Model of the Alveolar-Capillary Barrier to Investigate the Effect of Matrix Structure on Atelectrauma. Sci Rep. 2017;7(1):11623.
155. Lamers MM, Haagmans BL. SARS-CoV-2 pathogenesis. Nat Rev Microbiol. 2022;20(5):270-84.
156. Kusoglu A, Yangin K, Ozkan SN, Sarica S, Ornek D, Solcan N, et al. Different Decellularization Methods in Bovine Lung Tissue Reveals Distinct Biochemical Composition, Stiffness, and Viscoelasticity in Reconstituted Hydrogels. ACS Appl Bio Mater. 2023;6(2):793-805.
157. Hermanns MI, Unger RE, Kehe K, Peters K, Kirkpatrick CJ. Lung epithelial cell lines in coculture with human pulmonary microvascular endothelial cells: development of an alveolo-capillary barrier in vitro. Lab Invest. 2004;84(6):736-52.
158. Jain P, Nishiguchi A, Linz G, Wessling M, Ludwig A, Rossaint R, et al. Reconstruction of Ultra-thin Alveolar-capillary Basement Membrane Mimics. Adv Biol (Weinh). 2021;5(8):e2000427.
159. Viola H, Chang J, Grunwell JR, Hecker L, Tirouvanziam R, Grotberg JB, et al. Microphysiological systems modeling acute respiratory distress syndrome that capture mechanical force-induced injury-inflammation-repair. APL Bioeng. 2019;3(4):041503.
160. Wu J, Wang Y, Liu G, Jia Y, Yang J, Shi J, et al. Characterization of air-liquid interface culture of A549 alveolar epithelial cells. Braz J Med Biol Res. 2017;51(2):e6950.
161. Sen C, Freund D, Gomperts BN. Three-dimensional models of the lung: past, present and future: a mini review. Biochem Soc Trans. 2022;50(2):1045-56.
162. Dvorak A, Tilley AE, Shaykhiev R, Wang R, Crystal RG. Do airway epithelium air-liquid cultures represent the in vivo airway epithelium transcriptome? Am J Respir Cell Mol Biol. 2011;44(4):465-73.
163. Ohlinger K, Kolesnik T, Meindl C, Galle B, Absenger-Novak M, Kolb-Lenz D, et al. Air-liquid interface culture changes surface properties of A549 cells. Toxicol In Vitro. 2019;60:369-82.
164. Hoffmann W, Gradinaru J, Farcal L, Caul-Futy M, Huang S, Wiszniewski L, et al. Establishment of a Human 3D Tissue-Based Assay for Upper Respiratory Tract Absorption. Applied In Vitro Toxicology. 2018;4(2):139-48.
165. Costa A, de Souza Carvalho-Wodarz C, Seabra V, Sarmento B, Lehr CM. Triple co-culture of human alveolar epithelium, endothelium and macrophages for studying the interaction of nanocarriers with the air-blood barrier. Acta Biomater. 2019;91:235-47.
166. Kasper JY, Hermanns MI, Unger RE, Kirkpatrick CJ. A responsive human triple-culture model of the air-blood barrier: incorporation of different macrophage phenotypes. J Tissue Eng Regen Med. 2017;11(4):1285-97.

APPENDIX

APPENDIX 1

APPENDIX 1 (continue)

APPENDIX 2

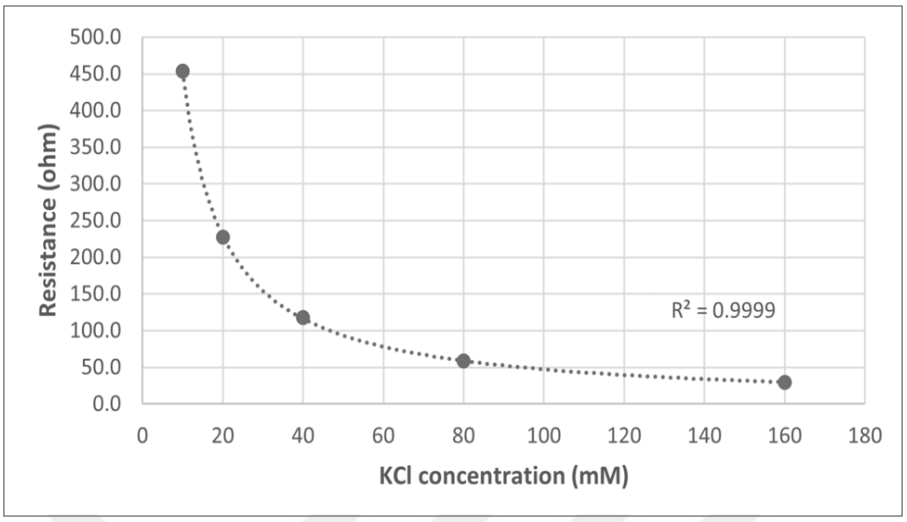

Figure 33 The change in the resistance of the medium with different KCl concentrations, measured using STX-4 electrodes

APPENDIX 3

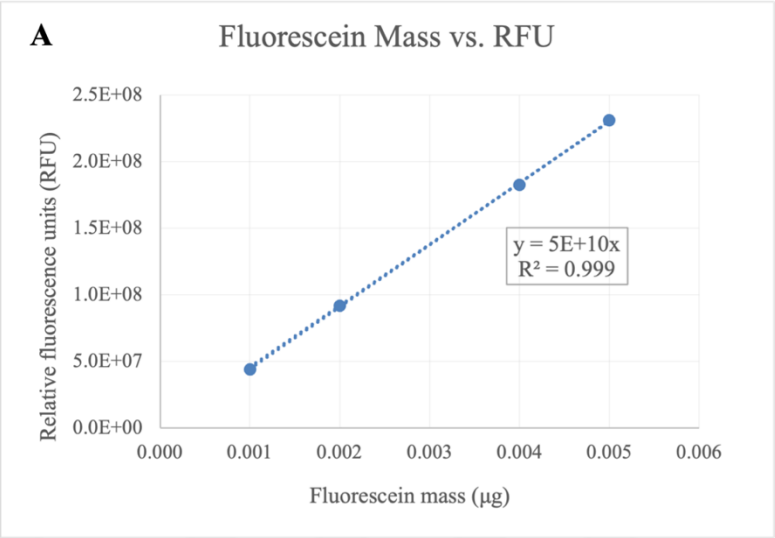

Figure 34 Relative fluorescence vs. mass standard curves plotted for fluorescein

9 CURRICULUM VITAE